3-D simulation of suppressed vortex shedding from bridge pier at high Reynolds number using attached splitter plate

Salar Kheshtgar Darvazeh

A Thesis

in

The Department

of

Building, Civil and Environmental Engineering

Presented in Partial Fulfillment of the Requirements

for the Degree of

Master of Applied Science (Civil Engineering) at

Concordia University

Montréal, Québec, Canada

November 2020

CONCORDIA UNIVERSITY

School of Graduate Studies

This is to certify that the thesis prepared

By: **Salar Kheshtgar Darvazeh**

Entitled: **3-D simulation of suppressed vortex shedding from bridge pier at high Reynolds number using attached splitter plate**

and submitted in partial fulfillment of the requirements for the degree of

Master of Applied Science (Civil Engineering)

complies with the regulations of this University and meets the accepted standards with respect to originality and quality.

Signed by the Final Examining Committee:

_____ Chair
Dr. Attila Michael Zsaki

_____ External Examiner
Dr. Ali Dolatabadi

_____ Examiner
Dr. Attila Michael Zsaki

_____ Supervisor
Dr. Samuel Li

Approved by _____
Dr. Ashutosh Bagchi, Chair
Department of Building, Civil and Environmental Engineering

_____ 2020

_____
Dr. Mourad Debbabi , Dean
Faculty of Engineering and Computer Science

Abstract

3-D simulation of suppressed vortex shedding from bridge pier at high Reynolds number using attached splitter plate

Salar Kheshtgar Darvazeh

Turbulent flow around in-stream bridge piers in open channels is complicated, with vortices and eddy motions of various length and time scales. These vortices cause significant channel-bed erosion and sediment transport, known as the scour problem. Consequences of scour include bridge failures, which can cause losses of property and, in some cases, of human life. Sediment scour from around the bridge piers has been a primary reason for all bridge failures and has incurred costs of millions of dollars to repair and rebuild. Researchers have tried to find ways to suppress vortices and reduce scour. They have suggested active and passive methods of suppressing vortices. One of the practical passive methods is to attach a splitter plate to the pier on either the downstream or the upstream side of the pier.

This research uses the computational fluid dynamic (CFD) method to simulate three-dimensional turbulent flow around a cylinder with or without an attached splitter plate. The objectives are to understand how effective the attached splitter plate is in reducing vortices, Turbulence Kinetic Energy (TKE), channel-bed shear stress around the cylinder, and to explore the optimal splitter plate length and direction. So far, detailed knowledge of the above-mentioned aspects is incomplete. This study provides a comparison of performance between splitter plates attached on the downstream and upstream side and having different lengths. The CFD simulations used the mesh-based numerical method, with sufficiently

fine resolutions for flow regions around the cylinder and near the channel-bed in order to capture detailed turbulence structures. The simulations solved the three-dimensional unsteady Navier-Stokes equations. The scope of work covers an assessment of the suitability of the shear-stress transport (SST) k-ω, the k-ω model, and the k-ϵ model for turbulence closure, as well as sensitivity tests to ensure the independence of numerical results on mesh configuration and time step.

The results show that a splitter plate fitted on the downstream or the upstream side of the cylinder can reduce drag and lift force coefficients. In particular, a downstream splitter plate with a longitudinal length of the pier diameter is the most desirable for minimizing the force coefficients. The downstream splitter plate can reduce TKE and channel-bed shear stress values by 38.7% and 32.81%, respectively. The downstream splitter plate shifts the peak TKE region further downstream, which has positive effect for in-stream pier stability. The force coefficients and TKE value are shown to compare well with the results from other studies reported in the literature. Splitter plates are shown to reduce cross-channel velocities in the channel-centre plane, compared to the case of no plate. The findings from this research are of practical values for the safe protection of bridge piers.

Acknowledgments

This thesis was completed in September 2020 at Concordia University in Montreal during the Covid-19 pandemic and it was encountered with my wedding day of 25th of September 2020. First of all, I would like to express my deepest appreciation to my supervisor Dr. Samuel Li for his endless support and encouragement during my M.A.Sc. study. This thesis could not be completed without his invaluable assistance and guidance. I would also like to thank Dr. Amruthur S. Ramamurthy for his helps.

Secondly, I send my greatest regards to my wife, Kimia Sepehrtaj who paves the way for me with her supports and unconditional trust on the days of writing my thesis. Also, I wish to express my gratitude to my parents and my brother with their unconditional support during my journey at Concordia University.

Special thanks to my friends, Rui Zeng, Pouya Nouri, Alireza Rahmati, Reza Ghobadpour and Pooya Abdolghader who went through hard times with me in the first months of arriving in Canada.

Contents

List of Figures

List of Tables

Chapter 1

Introduction

1.1 Background

Water flows in a river channel under the influence of gravity. If there is an obstacle in the flow path, the flow changes its direction in response. One significant instance is the flow patterns in river channels where there are bridge piers. Most of the bridge piers which have built in rivers are in cylindrical shape. Up on approaching the solid cylinder, the flow makes some changes in its path. The cylindrical body geometry is quite simple. However, the changing flow patterns are complicated. The complexity arises from such phenomena as flow separation, vortex shedding, and turbulence fluctuations. The pier structures are vulnerable to damage, if affected by strong, persistent vortices and severe turbulence. There have been many examples of damages to other types of structures by vortices and turbulence, including major fatigue damages to onshore wind turbine towers and offshore structures. Regarding bridge piers, the main problem has been river-bed sediment scour and bed erosion. Sediment scour occurs due to local increase in flow velocities near the bed boundary around the structure foundation.

There have been many cases of bridge failures caused by bridge pier scour. About 80% of all bridge failures around the world is because of scour around bridge piers Pasiok and

Stilger-szydlo (2010). Local scour caused 60% of an average of 50 to 60 bridges to fail per year in the United States Ettema, Melville, and Barkdoll (1998). More than 500 bridges were damaged by floods resulting from storm Alberto in 1994, and nearly one third of the failures were proved to be caused by scour damage Arneson (2013). In 1993, 23 bridges collapsed by floods in the upper Mississippi basin, of which 14 failures were due to scour. The damages from this flood were estimated to be about $15 million Wu, Balachandar, and Ramamurthy (2018). Nearly 70% of bridge damage costs in New Zealand were for repairing scour around the piers Melville (1997).

Scour can be characterized into two types: general scour or local scour. General scour is the transport of channel-bed materials due to seasonal changes or environmental conditions in flow velocity, or changes in channel shape or geological features. Local scour is caused by the presence of bridge piers or other obstacles in the flow. When these structures are constructed in the flow environment, they cause flow disturbances; these disturbances result in an increase in the transport of local sediments, triggering scour holes to develop. In spite of extensive research efforts on the issue of scour, scour-related failures of bridge structures remain problematic. There still is a lack of knowledge about the processes of scour. More significantly, there is insufficient research on finding applicable ways to reduce scour. A schematic sample of scour around a cylindrical pier presented in Figure 1.1 shows two kinds of vertices around bridge piers: a wake vortex which swirls horizontally and a horse-shoe vortex that rotates in the vertical direction. Furthermore, a photo of scour around an oval shape bridge pier is illustrated in Figure 1.2. Even if the flow is intermittent on the seasonal cycle and there is no or little flow of water in the dry season (Figure 1.2), the occurrence of a flood in the wet season can wash away the soil and sediments around the pier.

Turbulent flow around a bridge pier is very complicated with vortices and eddy motions of various length and time scales. With small variations in turbulence and bed shear

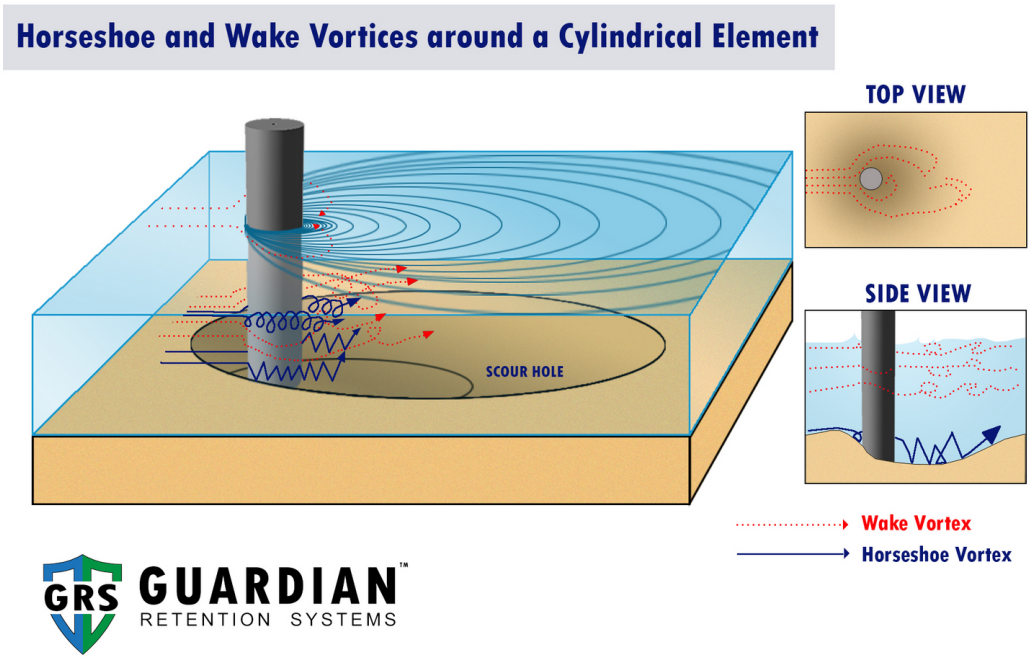

Figure 1.1: Schematic view of scour around a cylindrical pier. *https://guardianretentionsystems.com/bridge-piers/* (n.d.)

.

Figure 1.2: Scour hole around a bridge pier in a natural channel *www.researchgate.net* (n.d.)

.

stress, the scouring process becomes erratic in many folds. In three-dimensional turbulent flow, the number of unknowns is more than the number of physical-law-based equations, therefore it is impossible to solve for unknowns Wilcox et al. (1998). Field studies and experimental studies are very expensive and time consuming. Numerical modelling like Computational Fluid Dynamics (CFD) is an acceptable alternative approach.

The CFD approach can lead to an improved understanding of the processes of turbulent flow and vortices around bridge piers. Previously, researchers have tried to find ways to suppress these vortices and as a result, to minimize the scour depth. A review of the literature shows two main ways to suppress vortices for general applications (not limited to bridge pier scour problems): 1) active methods; 2) passive methods. The active methods used base-flow blowing Schumm, Berger, and Monkewitz (1994), base-flow suction Chen, Xin, and Li (2013), electrical heating of cylinder surface Lecordier, Hamma, and Paranthoen (1991) and optimal control Homescu, Navon, and Li (2002) etc. These methods appeared to be useful for suppressing vortices in laboratory experiments at low Reynolds numbers, but they were not practical in large scale applications due to excessive energy demands, high costs, a lack of resilience, and complexity. The passive methods were found to be applicable at large scale. The methods included the use of helical strakes Bearman and Branković (2004); Zhou, Razali, Hao, and Cheng (2011), ribbons Kwon, Cho, Park, and Choi (2002) and base splitter plate Apelt and West (1975); Dai et al. (2018); Dash, Triantafyllou, and Alvarado (2020); Soumya and Prakash (2017).

Among the above-mentioned methods for suppressing vortices, a splitter plate attached to a cylinder are useful. This is a simple device and easy to implement to new and existing bridge piers of large scale. The questions are: Is there an optimal longitudinal length (L) for the splitter plate attached to a pier of diameter (D)? In other words, what should the (L/D) be for the maximum suppression of turbulence?. Is it better to attach a plate to the pier on the upstream side or the downstream side? How do turbulence characteristics

change in response to the presence of a plate? These questions provide the context of this research.

1.2 Objectives

The objectives of this thesis study are:

- to achieve an improved understanding of the 3-D turbulent flow structures around a circular bridge pier;
- to reveal how the flow structures respond to the presence of a splitter plate attached to the circular bridge pier; and
- to find the optimum plate length and direction in order to minimize the drag and lift force coefficients, turbulence kinetic energy (TKE) and channel-bed shear stress in the vicinity of the bridge pier.

1.3 Contributions from this work

The contributions from this work can be summarized as:

- an improved understanding of the effects of a splitter plate on the suppression of flow turbulence around a pier in open channels;
- exploration of computational strategies for simulations of flow around a pier and the demonstration of proper turbulence closure method for modelling flow around a pier;
- quantification of the difference in turbulence characteristics between splitter plates fitted on the downstream and upstream sides of the pier.
- detailed predictions of near-bed TKE and channel-bed shear stress, which are the key factors in studies of channel-bed sediment scour;

- the creation of new knowledge that a splitter plate fitted on the upstream side of the cylinder is more capable of reducing the drag coefficient $\overline{C}_D$ than a splitter plate fitted on the downstream side.

1.4 Organization of the thesis

The rest of this thesis is organized as follows in order to achieve the above-mentioned objectives.

Chapter Two gives a review of turbulent flow and bridge pier scour processes. The review of the literature covers experimental, numerical and analytical research work on the topic of flow and scour around bridge piers as well as proposed methods for suppression of vortices in the vicinity of bridge piers. Notable progress that have been made from the previous researchers will be discussed.

Chapter Three presents the governing equations in modelling flow and computational methods for different turbulence closure, including the k-ϵ, the k-ω model, and the SST k-ω model. This chapter discusses the advantages of the SST k-ω as the choice of turbulence closure in this study. Additionally, this chapter describes the computational domain, mesh, boundary conditions and control parameters used in this thesis.

Chapter Four discusses the results from CFD modelling, along with comparisons of the CFD results with data from other independent sources. This chapter begins with discussion of sensitivity test results, followed by the results of average drag coefficients $\overline{C}_D$ and fluctuating lift coefficients C_l'. Discussions of the results cover such important variables as TKE, channel-bed shear stress, turbulent eddy viscosity and frequency, and secondary flow in the cross-channel direction.

Finally, Chapter Five give highlights of concluding remarks from this study. The highlights emphasise on the beneficial effects of a splitter plate fitted to a cylinder on suppressing vortex shedding and scour potential. This chapter makes suggestions for future studies

on the topic of using splitter plates of various lengths for turbulence suppression in more realistic channel geometry.

Chapter 2

Literature Review

2.1 Description of turbulent flow

The velocity of water flow around bridge piers fluctuates in time and varies in space. The flow is defined as turbulent in open-channel hydraulics when the Reynolds number, Re, is high (Re$\geq$3000). At high Reynolds number, disturbances not only do not stops but also are amplified Bradshaw (2003). Turbulent flow contains considerable vorticity and is dominated by inertial forces which yields chaotic eddies, vortices and other flow instabilities.

2.2 Bridge scour process

Richardson and Davis (2001) suggested that the most common cause of bridge failures is the the local scour around bridge piers. The three dimensional flow around a circular pier is presented in Figure 2.1.

Just upstream of the pier where the flow reaches the pier, the flow divides into two parts. One part goes to upward direction and the other goes to downward direction. The

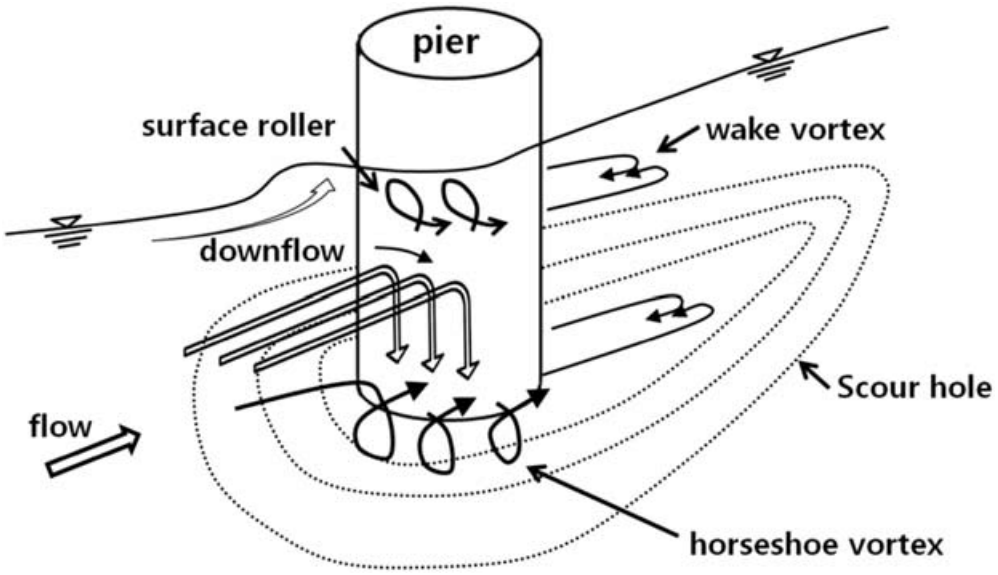

Figure 2.1: Representation of flow around a circular pier Choi and Choi (2016).

upward flow forms a bow-wave circulation. The downward flow driven by a strong pressure gradient causes a horseshoe vortex at the riverbed. This is destructive and one of the consequences is the formation of scour holes. Since the rate of sediments removed away from the pier base is greater than the rate of sediments supplied from upstream, a scour hole develops gradually until an equilibrium is reached Richardson and Davis (2001). The equilibrium is defined as the time that velocity of flow circulation inside the scour hole is incapable of removing bed sediments from the hole or the time that the rate of sediments transporting inside the hole is equal to sediments removed from the scour hole. The wake vortices occur in addition to the horseshoe vortex which rotates horizontally at the downstream of the pier. Both of these vortices cause a degradation on the riverbed and removed sediments from around the pier region.

2.3 Flow and pier scour investigation

The sediment erosion around bridge piers have been a difficult issue to deal with, therefore, scholars and scientists have tried to model and understand the process of scouring around piers. Previous investigations include experimental and numerical approaches to understand the velocity field, turbulence, bed shear stress, and vortex shedding around bridge piers.

2.3.1 Experimental investigations

Investigators have used a wide variety of laboratory experiments. Sadeque, Rajaratnam, and Loewen (2008) studied the flow around circular objects in an open channel. Four piers of cylindrical shape with the same diameter but different heights were tested under a similar flow condition. Four different levels of submergence, including a surface piercing bridge-pier-like cylinder were investigated. The flow characteristics like bed shear stress were identified using a set of visualization tests. The results showed that the destructive horse-shoe vortices were found to appear closer to the submerged cylinders in comparison to a surface piercing cylinder. The bed shear stress was found to decreased with increasing level of submergence. Ettema, Kirkil, and Muste (2006) investigated a local scour at different size piers that were placed in a sand bed. The outcomes revealed that there was a direct relationship between the cylinder diameter and the scour depth. The authors argued that the cylinder diameter, bed sediment size, and flow depth should be taken as a three independent factors in laboratory experiments. Recently, Dias, Fael, and Nunez-Gonzalez (2019) focused on the effect of debris carried by natural streams on the maximum scour depth. This was neglected in the most recent studies. The experiments paid special attention to the development of scour hole as the accumulated debris increased. The focus of the laboratory experiments was on the development of scour hole by gradually accumulating debris around bridge piers. The results revealed that the accumulated shape and the position of

the debris had significance impacts on the final scour depth. The triangular shape debris on the bottom and upstream of the pier acted as a scour countermeasure, reducing the maximum scour depth up to 26% in their experiments. Using high-resolution Particle Image Velocimetry (PIV), Guan, Chiew, Wei, and Hsieh (2019) tried to obtain and investigate the detailed turbulent flow and the development of the horseshoe vortex in a developing scour hole around bridge pier. They also presented the distributions of the velocity field, turbulence intensities, and Reynolds shear stresses of the horseshoe vortex in their study. The main findings were: 1) The region of the maximum turbulence intensity and the maximum Reynolds shear stress occurred upstream of the main vortex, in the place where the largest turbulent eddy is expected to occur; 2) The horseshoe vortices evolved from a small vortex upstream of the pier and developed into three vortices at equilibrium. Dargahi (1989) experimentally investigated a cylinder of circular shape on a flat bottom at Reynolds numbers between 6600 and 65000. The author reported that the number of vortices and the flow patterns in the wake of the cylinder depended on the Reynolds number. The author also observed that wake vortices disappeared downstream of the cylinder. Graf and Istiarto (2002) studied the three-dimensional flow field around a cylinder was placed in a scour hole. They used an Acoustic-Doppler Velocity-Profiler (ADVP) to measure velocity components in a vertical plane upstream and downstream of the cylinder. The results showed that a vortex system and a strong turbulence, formed at the wake of the cylinder.

2.3.2 Numerical investigations

Using Large Eddy Simulation (LES) , Yen et al. (2001) tried to model flow velocity and the river-bed evolution under scouring condition around circular piers. Then, they compared LES flow velocity with the results of Laser Doppler Velocimeter (LDV) measurements made by Yeh (1996). They also compared the final scour levels obtained from LES with the laboratory measurements of Yeh (1996). The LES result agreed well with the

experimental data. The modelled and measured velocity fields and bed-level contours from the researches are shown in Figure 2.2 and 2.3, respectively.

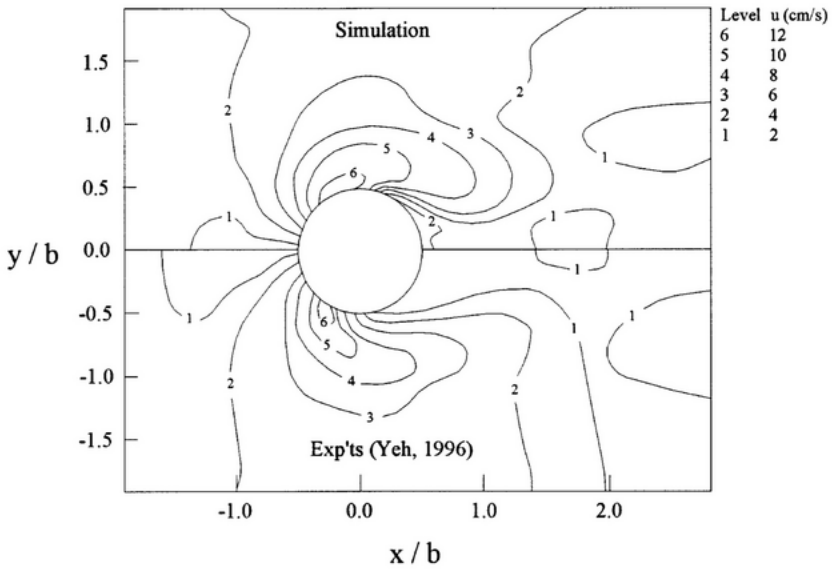

Figure 2.2: simulated velocity field (upper half) and measured (lower half) Yen et al. (2001).

Huang, Yang, and Xiao (2009) carried out a numerical simulation to access the scale effect on turbulent flow and sediment scour around cylindrical bridge pier by using (FLUENT 2007). The results of flow and scour were obtained using two different approaches: a) Physical modelling based on Froude number similarity; b) three-dimensional CFD modelling. In the physical modeling the effect of turbulent Reynolds number is ignored. The CFD model uses the 2nd order turbulence model to calculate turbulent velocity and sediment scour. The results from the three-dimensional CFD model were compared with the physical modelling. The authors concluded that the predicted flow patterns around a circular cylinder using Fluent were better than the results from Froude number similarity.

Salaheldin, Imran, and Chaudhry (2004) used FLUENT to simulate the separated turbulent flow and bed shear stress around a circular pier using different turbulence models and compared them with experimental results available in literature. The authors reported poor

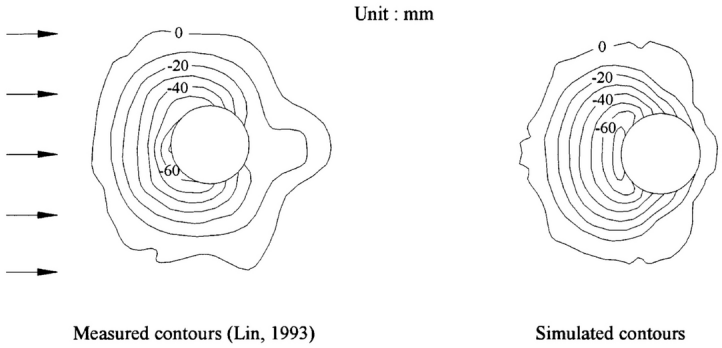

Figure 2.3: Compared final bed elevation Yen et al. (2001).

performance of $k-\varepsilon$ in estimating near-bed shear stress but satisfactory performance in producing velocity profile results, despite commonly perceived weakness of the $k-\varepsilon$ model in simulating 3D open channel flows. Moreover, the Reynolds stress model produced the most acceptable results of velocity profiles, bed shear stress in flat bottom channel around a circular cylinder. Ali and Karim (2002) used FLUENT to model the three-dimensional flow field around a circular cylinder. The goal of their study was to find an expression of scour depth as a function of time using the variation of bed shear-stress around the cylinder. The results showed that the scour depth was dependent of three dimensionless numbers: 1) the sediment size number around the cylinder; 2) the pile number; 3) the duration time number. Moreover, the magnitude of TKE was reported to be a significant contributor to scouring. Jia et al. (2018) simulated a local scouring around bridge piers and reported that the powerful turbulent fluctuations and the down-flows around the cylinder were significant factors to bed scouring. Furthermore, they extracted scour hole contours and compared them to the experimental results 2.4.

Using Reynolds-averaged Navier-Stokes Equation $k-\epsilon$ approach, Zaid et al. (2019) modelled three dimensional flow around a bridge pier fixed on a flat bed. The main purpose of their study was to validate the model against available experimental data. The validations

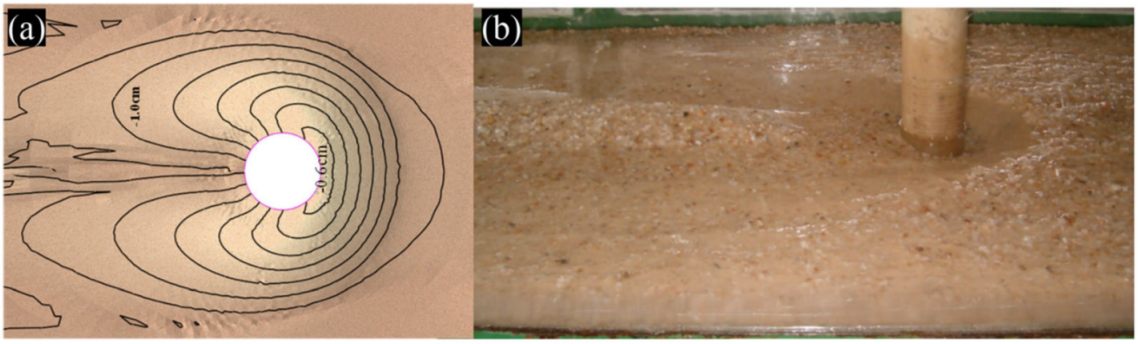

Figure 2.4: Contours of the simulated scour hole (left) and the live-bed photograph (right) Jia et al. (2018)

proved that the CFD modelling approach is reliable in reproducing flow characteristics around bridge piers of different shapes. The average velocity contours at the Reynolds number of 39000 are shown in Figure 2.5. In panel (d) the wake of the cylinder is visible in blue color.

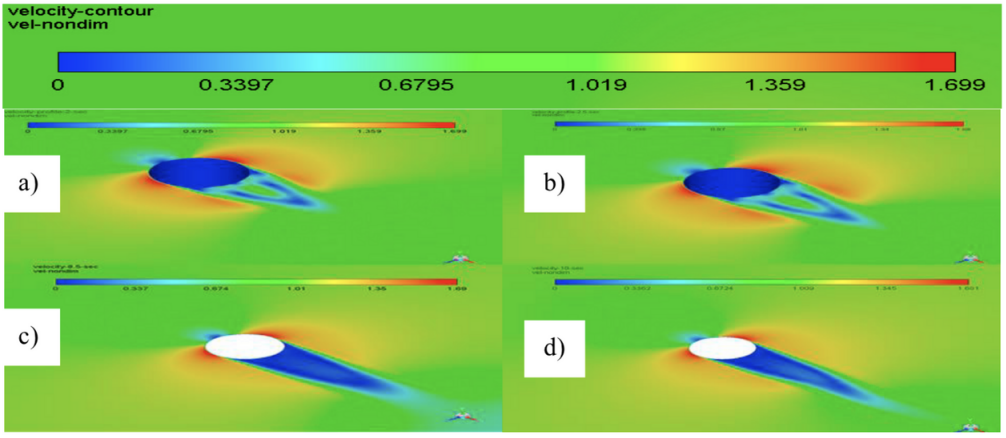

Figure 2.5: Velocity field contours for different time steps Zaid et al. (2019)

2.4 Modelling flow around multiple bridge piers

Some of the bridge abutments in rivers have multiple cylindrical piers in a row. These piers can be exposed to scouring all over the year, especially during the flood season. Figure 2.6 shows the scour around multiple abutment piers of cylindrical shape due to their exposure to scouring.

Figure 2.6: Scouring around an arrangement of cylindrical piers Pasiok and Stilger-szydlo (2010)

Da Silva et al. (2019) numerically investigated a 3D flow around cylinders in different arrangements at critical Reynolds number using LES. Their goal was to evaluate flow characteristics and patterns, in addition to TKE and force coefficients like C_D and C_l' for each of arrangements. The numerical results were in good agreement with the experimental data in the literature. The computational domain including the four different arrangements of cylinders and the normalized TKE are shown in Figure 2.7 and 2.8, respectively.

For the case showing in panel (a) 2.8, the TKE was very low at the first two rows but

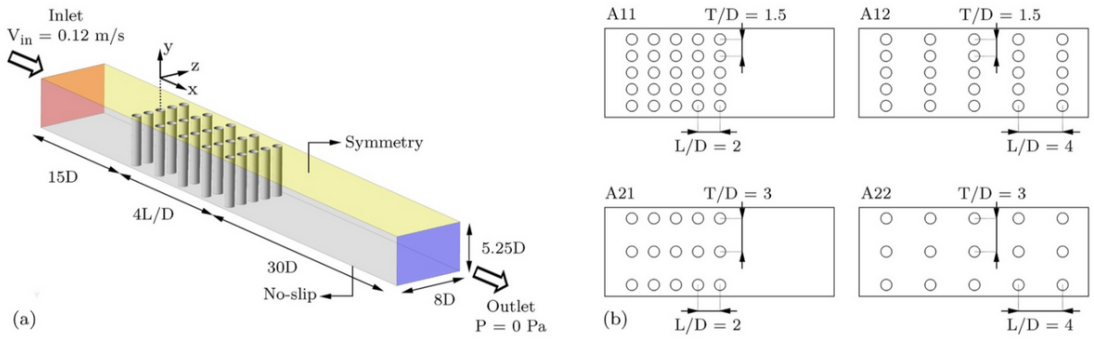

Figure 2.7: Computational domain and different arrangements of cylinders Da Silva et al. (2019)

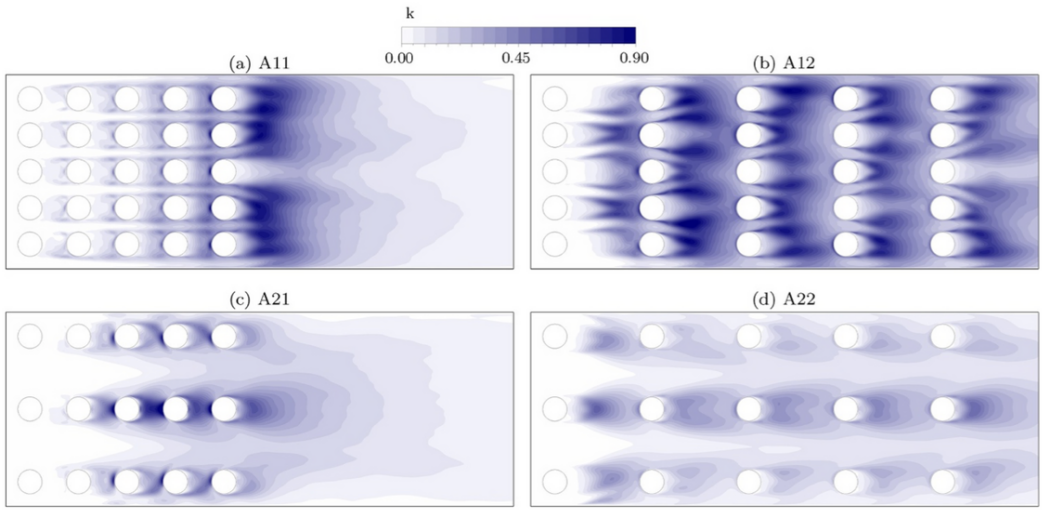

Figure 2.8: Normalized TKE for the different arrangements Da Silva et al. (2019)

increased from the fourth row and reached the maximum at the fifth row. This is due to vortex shedding effects. In panel (b), the TKE was approximately the same, except in the first row where TKE was high. Panels (c) and (d) shows relatively high intensities of TKE at the middle cylinders due to a lack of wall interference. Overall, the cylinder rows of panel (d) performed better in terms of the TKE intensity compared to the other arrangements.

2.5 Vortex suppression using splitter plates

After realizing the destructive effects of vortices around bridge piers, researchers tried to find ways to suppress these vortices and ultimately reduce or eliminate scouring. The simplest, cost-effective and most applicable way to suppress vortices is to use splitter plates either at the upstream or the downstream of the piers. Many researchers simulated the flow around a circular pier with a splitter plate experimentally or numerically.

2.5.1 Downstream splitter plate

De Araujo et al. (2018) used two-dimensional (2D) numerical simulations to model a cylinder fitted with a splitter plate of different lengths. They covered Reynolds numbers of 100, 160, 300 and 1250. They compared the Strouhal number, $\overline{C}_D$ and C_l' to each other in order to find the optimum plate length. The results showed the splitter plate was effective in attenuating the vortex shedding. When the flow is laminar ($Re \leq 300$), the flow characteristics were reported to be dependant of the splitter plate length. However, below the critical Reynolds number ($Re = 1250$) the splitter plate length was less influential. Figure 2.9 shows the streamlines in the wake of cylinders. The authors reported that when the splitter plate length was $L/D = 1$, vortices shifted location towards downstream.

Abdi et al. (2017) conducted 2D modeling of a cylinder fitted with up to 3 splitter plates on the wake side. The splitter plate length was fixed to the cylinder diameter. They also

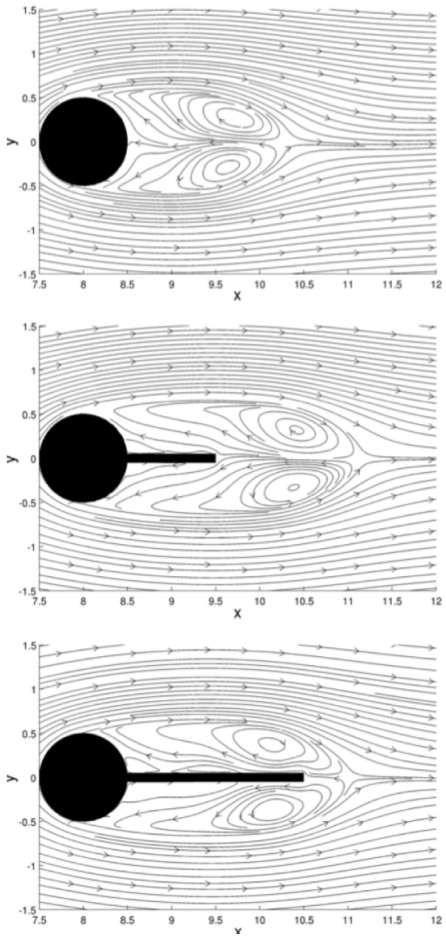

Figure 2.9: Streamlines of flow with and without splitter plate De Araujo et al. (2018).

investigated the force coefficients. The positions of splitter plates are shown in Figure 2.10. The results showed that an increase in the number of splitter plates from 1 to 2 caused a decrease in the drag coefficient, Strouhal number and C_l'. However, a further increase in the number of splitter plates did not have substantial effect on those quantities. In the case of a single splitter plate, the minimum Strouhal number was observed when the angle of attached splitter plate was zero degree. Overall, the results of their study suggested that the vortex shedding frequency, C_D,C_l' and strouhal number could be substantially decreased with using one or more splitter plates.

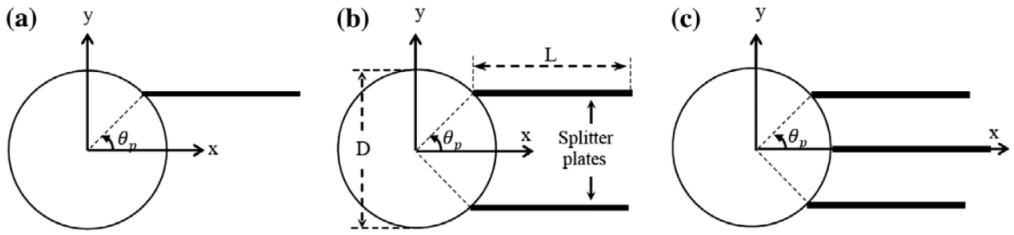

Figure 2.10: The position and the angle of the plates for Abdi et al. (2017)

Akilli et al. (2008) experimentally studied passive control of vortex shedding by using splitter plates of different lengths from $L/D = 0.2$ to $L/D = 2.4$ at $Re = 6300$. The results revealed that the turbulent flow characteristics such as TKE, Reynolds shear and normal stress were highly affected by the length of the splitter plates and drastically changed up to $L/D = 1.2$. However, above this plate length, changes were small. Up to $L/D = 0.6$, the vortex shedding frequency was highly reduced and the large-scale vortex shedding at the wake of the cylinder completely vanished when the splitter plate length was larger than critical length $L/D = 1.2$. The TKE and normalized Reynolds shear stress contours are shown in Figure 2.11 and 2.12, respectively.

Dai et al. (2018) studied both 2D and 3D flows at the fully turbulent regime and investigated the dependence of vortex-shedding suppression on the ratio of splitter-plate width and height to cylinder diameter and length. First, a 2D flow was modelled in order to find

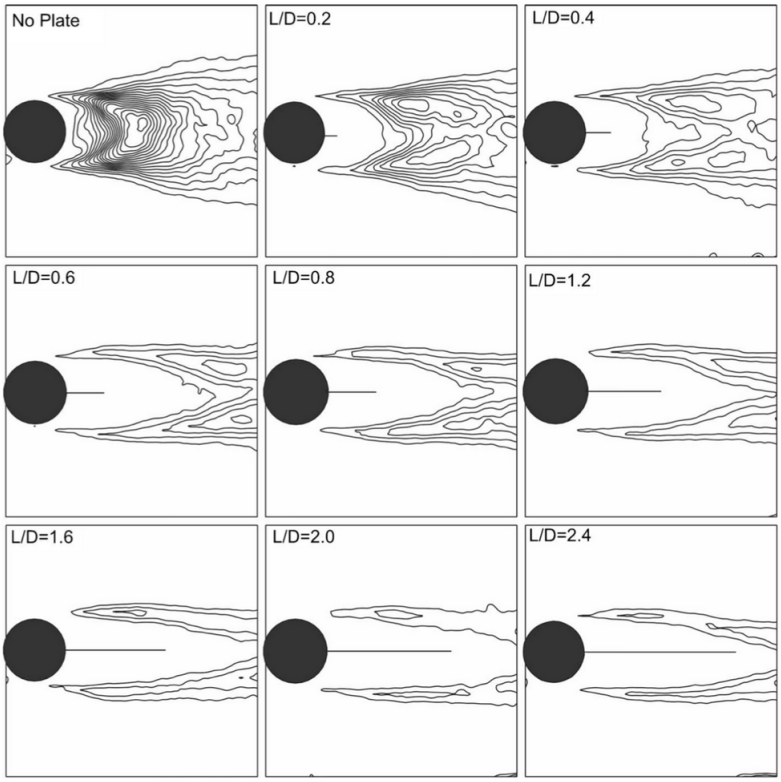

Figure 2.11: TKE cotours for different splitter plate length Akilli et al. (2008)

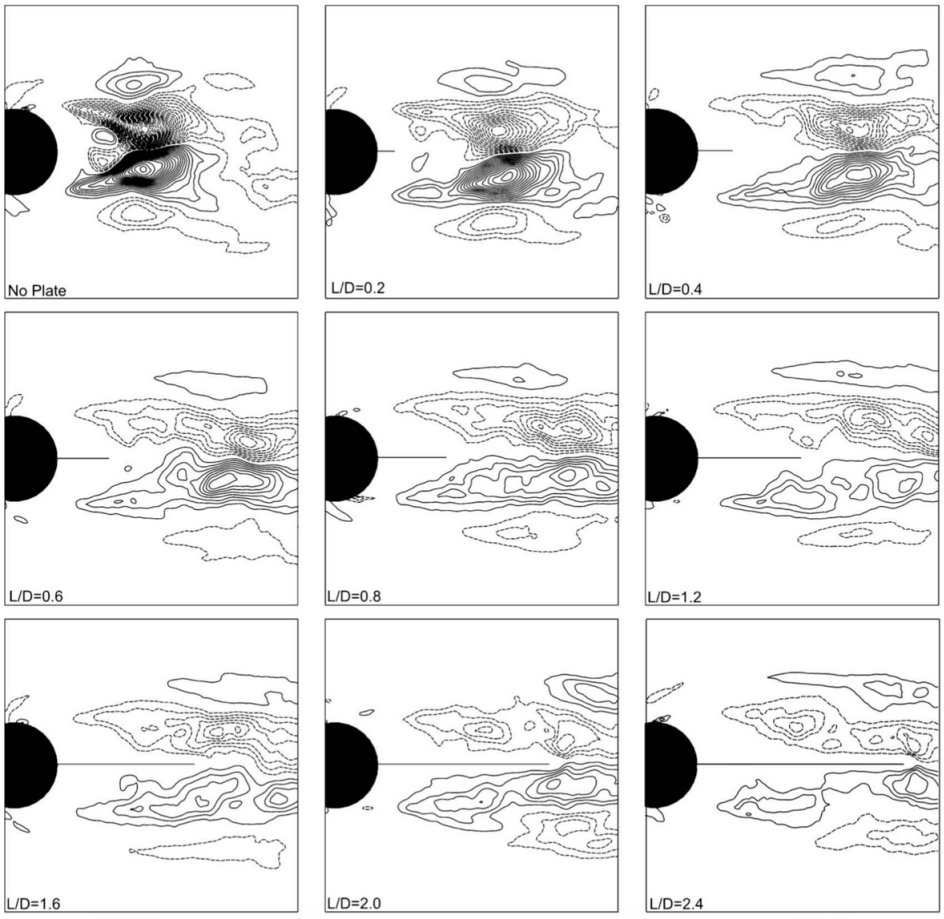

Figure 2.12: Normalized Reynolds shear stress for different splitter plate lengths at the bed surface Akilli et al. (2008)

an optimum plate length (W) to cylinder diameter (D). The results indicated that splitter plates provided a real solution for vortex suppression at high Reynolds number. When the ratio of splitter plate width (W) to cylinder diameter (D) was $0.5 < W/D < 0.75$, the degree of suppression could be maximized. Therefore, the authors decided to hold the condition of $W/D = 0.6$ and find the optimum plate height (H) to cylinder length (L) with the ratio varying between $0 < H/L < 1$ using 3D numerical modelling. For clarification, the domain and boundary conditions are shown in Figure 2.13. When $H/L = 1$ which means a cylinder with a full length splitter plate, the C_D and C_l' showed the minimum values. The results of C_l' for the 2D modelling case, which showed the degree of vortex suppression, are shown in Figure 2.14.

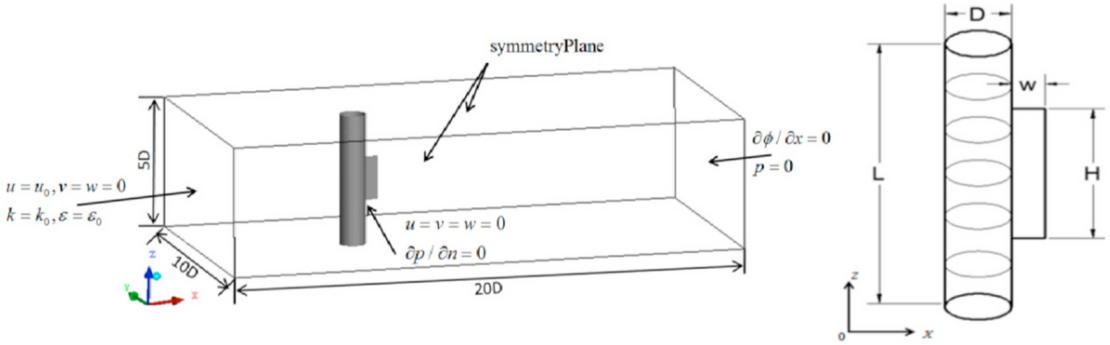

Figure 2.13: Domain and boundary conditions Dai et al. (2018)

Therefore, for fixed W/D of 0.6, the ratio of splitter-plate height (H) to cylinder length (L) was investigated. The results revealed that the optimum value was $H/L = 1$. Vu, Ahn, and Hwang (2015) investigated the effects of splitter plate of different lengths on the flow characteristics like vortex shedding, drag coefficient, lift coefficient, separation angle, pressure, and friction coefficients of the cylinder at several Reynolds numbers. The results revealed that the vortex shedding could be completely suppressed in the case that the splitter plate length was longer than the critical value. This value is proportional to the Reynolds

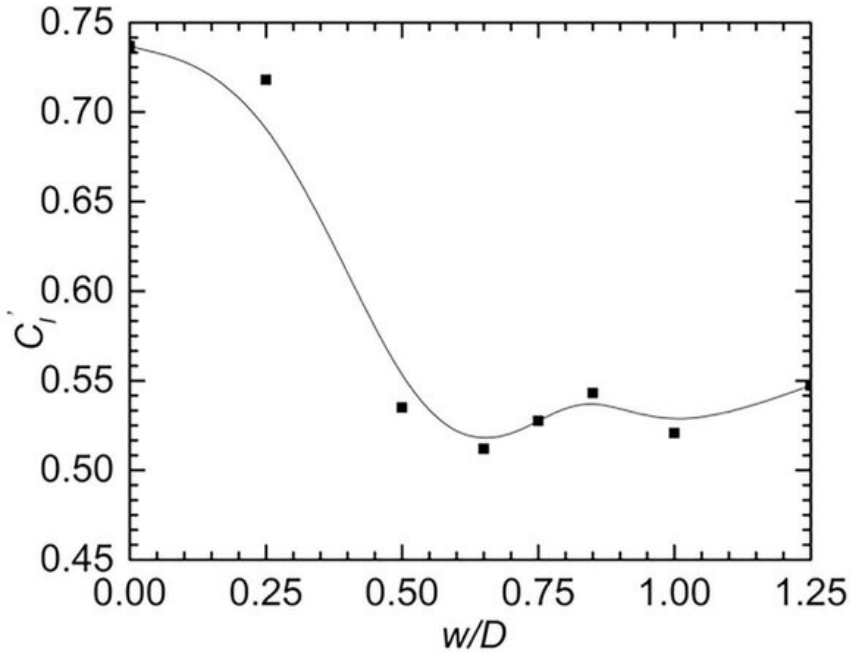

Figure 2.14: Fluctuating lift coefficient with variation of W/D Dai et al. (2018)

number. De Araujo, Camano Schettini, and Silvestrini (2016) performed a direct numerical simulations of a cylinder with a fixed plate of up to twice of the cylinder diameter at $Re = 1250$. The results revealed that the splitter plate was effective in suppressing the turbulence intensity, which was in a good agreement with the experimental data. Furthermore, the vortex shedding frequency was reduced by 5% . Shaligram, Chakraborty, Gautam, and Pradipta (2005) performed a numerical study to analyze the effect of the downstream splitter plate on the flow characteristics. They showed that using splitter plate could change the wake characteristics and also decrease the size of the wake.

Liu et al. (2016) carried out an experimental study to investigate the effect of a splitter plate on the downstream of the cylinder which was placed symmetrically in submergence in a channel. PIV measurements were used to capture the flow structure and to analyze the vortex shedding process. The Reynolds number was from 2400 and 3000. The results showed that the splitter plate was capable of stabilizing wake turbulence. For the splitter

plates of $L/D = 0.5$ and 0.75, the vorex shedding frequency decreased and the flow structures were significantly modified, in comparison to a bare cylinder. For the splitter plates from $L/D = 1$ to 1.5, the secondary vortex was generated based on the snapshot proper orthogonal decomposition (snapshot POD). Moreover, the TKE and Reynolds shear stress became minimum and the vortex shedding frequency disappeared. The TKE along the center line of the domain is shown in Figure 2.15. At both of the Re numbers, adding a splitter plate could significantly reduce the peak of TKE around the cylinder, especially for longer length of splitter plates ($L/D = 1, 1.25$ and 1.5. From Figure 2.15 the authors made the conclusion that the optimal length of splitter plate length was $L/D = 1$.

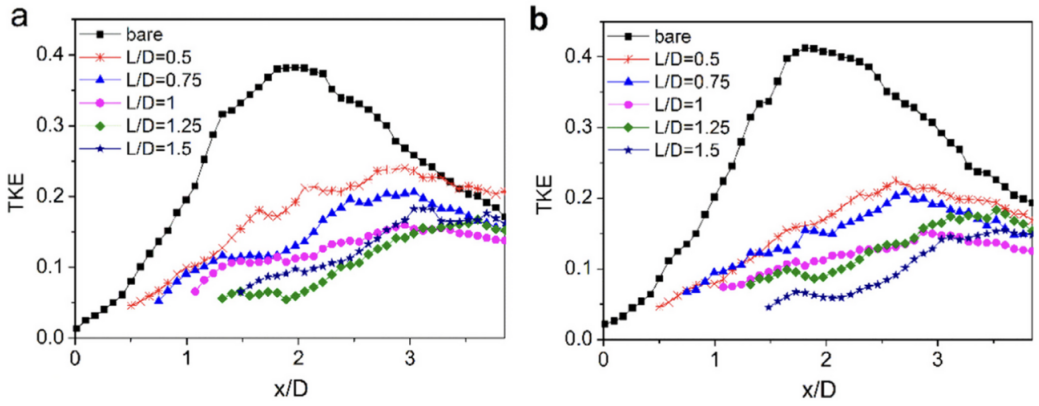

Figure 2.15: Variation of normalized TKE along the wake centerline at (a) $Re_D = 2400$ and (b) $Re_D = 3000$ (Liu et al. (2016))

.

An et al. (2019) utilized two-dimensional unsteady incompressible Reynolds-averaged Navier-Stokes (URANS) equations at the Reynolds numbers from 5×10^4 to 9×10^4 to investigate the effect of different length of splitter plate on the wake of cylinder. The turbulence closure used was SST $k - \omega$ with three different grid resolutions. The computational domain and boundary conditions are shown in Figure 2.16. The boundary conditions of this study are similar to the boundary conditions of our study. It was revealed that the vortex

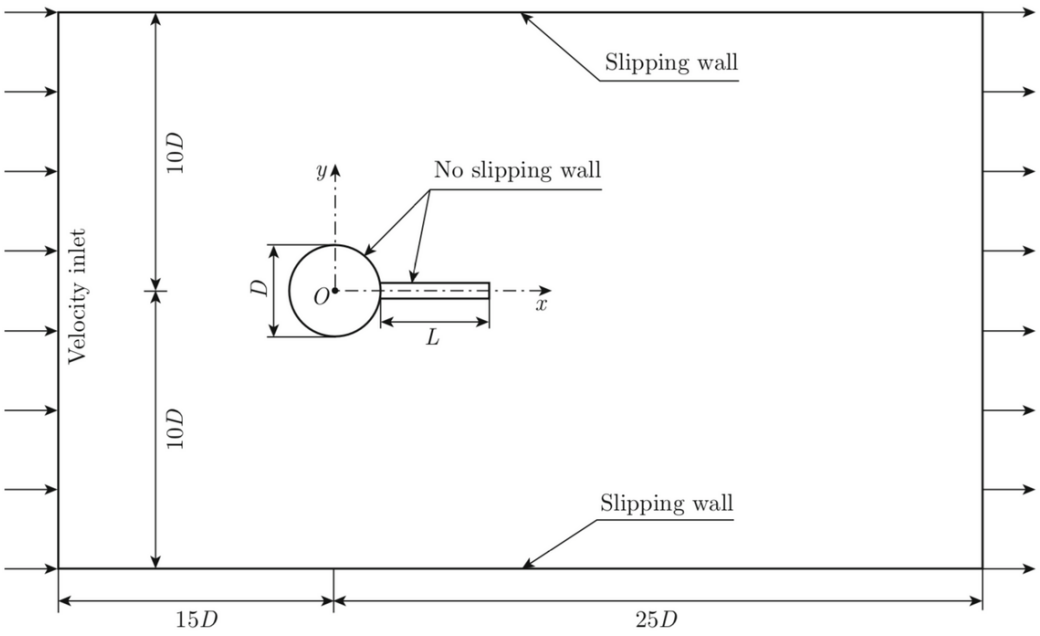

Figure 2.16: Computational domain and boundary conditions from top view An et al. (2019)

.

shedding was strongly suppressed when the splitter plate length was longer than a critical value. Furthermore, the lift coefficient reached the maximum value when the splitter plate length was 2 times of the cylinder diameter. The separation angle was reportedly not dependant of the splitter plate length.

Ozkan, Firat, and Akilli (2017) investigated the suppression of the vortex shedding using an attached permeable splitter plate. Two important parameters of their study were porosity β and the angle between the plate and freestream θ. The results revealed that using the permeable plate could successfully suppress the vortex shedding at the wake of the cylinder and elongate the vortex formation further downstream. The maximum TKE and C_D were reduced for almost all of the porosity ratios when $\theta < 30°$.

2.5.2 Upstream splitter plate

Using the PIV measurements, Chutkey et al. (2018) studied the flow past a circular cylinder with upstream splitter plates at the Reynolds number of $5.1 * 10^4$. The length of the splitter plate was adjusted to the cylinder diameter $(L/D = 1)$. The results showed a 22% reduction in streamwise velocity fluctuations, in comparison to the bare cylinder. Furthermore, the upstream splitter plate substantially changed the wake characteristics, reduced C_D by 13%, and delayed the flow separation. More importantly, the depth averaged velocity from PIV measurements indicated that the strength of vortices was weaker in the upstream splitter plate (labeled as FSP) cylinder in comparison to a plane cylinder. The Reynolds stress decreased by 34% as shown in Figure 2.17. Panel (a) is for the plane cylinder, which reveals two symmetrical regions of high Reynolds stress (red and blue) just behind the cylinder. However, panel (b) shows two regions of low Reynolds stress (light red and light blue colors), which means the Reynolds stress is lower than the bare cylinder.

Khaple, Hanmaiahgari, Gaudio, and Dey (2017) experimentally investigated the upstream splitter plate's capability in reducing the maximum scour depth. The plate was attached at the upstream vertical plane of symmetry. Two kinds of sediment sizes ($d_50 = 0.96$ and $1.8mm$) and multiple combinations of splitter plate lengths and thicknesses were considered. The results indicated that with a increasing splitter plate length, the maximum scour depth decreased consistently. However, the scour depth was independent of splitter plate thickness. The best combination of splitter plate length and thickness was $2D$ and $D/5$, respectively. Moreover, the splitter plate could deflect the flow and therefore weaken TKE, vortex shedding and horseshoe vortices.

In summary, key results from previous studies are impressive, including: 1) Splitter plates can effectively suppress vortex shedding and decrease scour hole depth; 2) Downstream splitter plates have been most often used as methods for suppressing vortex shedding. However, there are some knowledge gaps that need to be filled. The most important

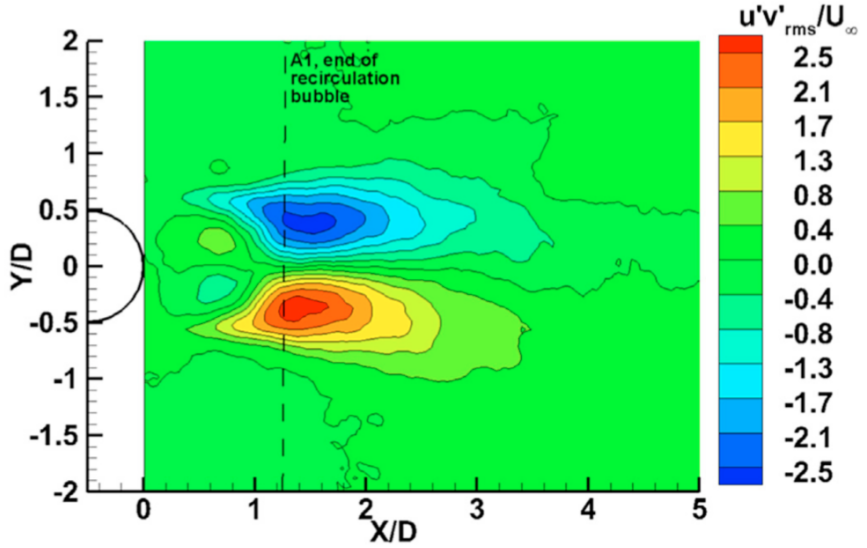

(a) Plain cylinder case

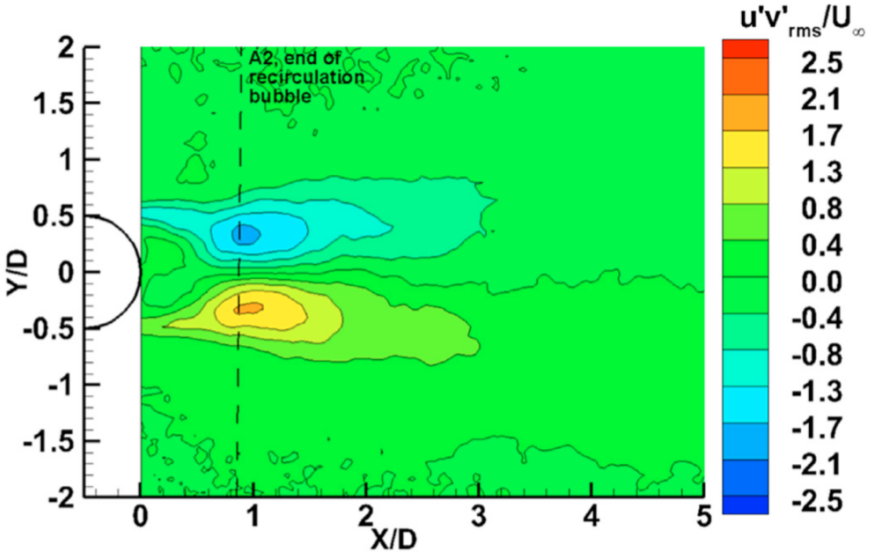

(b) FSP cylinder case

Figure 2.17: Time averaged contours of Reynolds stress Chutkey et al. (2018)

.

gap is that most of the previous modellings are 2D at low Reynolds number. Another important gap is a lack of comparing upstream and downstream splitter plate under the same flow configuration. To our best knowledge, the present study is the first study that considers 3D, high Reynolds number, cylinders with full length splitter plates at both upstream and downstream sides.

Chapter 3

Methodologies

3.1 Introduction

Computations of three-dimensional transient turbulent flows can be performed using direct numerical simulation (DNS), large eddy simulation (LES), or simulation based on the Reynolds-averaged Navier-Stokes momentum and continuity equations. In DNS, the spatial and temporal resolutions must be so small that they resolve fluid motions down to the Kolmogorov length, time and velocity scales. Currently, applications of DNS are limited to low Reynolds number flows. In LES, which was introduced by Smagorinsky (1963), the cell is required to be sufficiently fine to capture most of the energy-bearing motions. Furthermore, the time-step size should be minimal compared to the time scale of the vortex shedding process when considering the stability of explicit differencing schemes. Because of the high computational cost of LES as Reynolds number (Re) increases, most LES investigations have been performed at low Re numbers. The Re number used in this study is high (similar to river condition). Therefore, the LES method is not computationally efficient for simulations of this study.

In this study, computations of the flow field were performed using the unsteady Reynolds-averaged Navier-Stokes (URANS) equations. This computational approach incurs considerably lower costs than the DNS and LES approaches. In the URAN approach, it is important to determine both the appropriate time step and control volume size. The solutions should be free of dependence on cell and time-step sizes. Although the computing power has increased noticeably during the last decades, the URANS approach has remained to be the most commonly used approach in CFD applications as it offers the most economical numerical solutions to industrial and engineering problems of complex turbulent flows.

The URANS approach requires the use of a model for turbulence closure. Commonly used turbulence closure models include: the $k-\epsilon$ model (Jones and Launder (1972)), the $k-\omega$ model (Wilcox (1993)), and the shear stress transport (SST) $k-\omega$ model (Menter (1994)). This study made a comparison of performance among these three turbulence closure models. Previously, some numerical studies of turbulent flows demonstrated the advantage of SST $k-\omega$ model. It has been reported that the $SSTk-\omega$ model produces more accurate results of flow in a near-wall region than the other two turbulence closure models. The governing equations of these turbulence closure models are given in Sections 3.3 - 3.5. Nguyen, Ahn, and Park (2018) used the three mostly used turbulence closure models, namely the $k-\epsilon$, $k-\omega$, and SST $k-\omega$ in modelling flow around a scour hole. The results showed that the SST $k-\omega$ was the most suitable turbulence closure model for simulating flow around scour holes.

In this study, the finite volume code ANSYS Fluent 19.2 (*ANSYS 2019b* (n.d.)) was used to solve the URANS equations. Concordia University's High-Performance Computing (HPC) Facility (*Concordia HPC* (n.d.)) was used to run the cases of this study. This chapter represents a description of the turbulence closure model equations and the governing URANS equations. This chapter also presents the imposed boundary conditions.

3.2 Governing equations

Let (u, v, w) denote the three orthogonal components of the instantaneous velocity in the x-, y-, and z-directions, the continuity equation for an incompressible fluid flow is given by:

$$\frac{\partial u}{\partial x} + \frac{\partial v}{\partial y} + \frac{\partial w}{\partial z} = 0 \tag{1}$$

By using Reynolds decomposition, the instantaneous velocity components can be split into time-averaged velocity components (U, V, W) (or the mean flow components) and velocity fluctuations (u', v', w') as below:

$$u = U + u', \tag{2}$$

$$v = V + v' \tag{3}$$

$$w = W + w' \tag{4}$$

The momentum equations for an open-channel flow are as follows:

$$\rho\left[\frac{\partial u}{\partial t} + u\left(\frac{\partial u}{\partial x} + \frac{\partial v}{\partial y} + \frac{\partial w}{\partial z}\right)\right] = -\frac{\partial p}{\partial x} + \mu(\frac{\partial^2 u}{\partial x^2} + \frac{\partial^2 u}{\partial y^2} + \frac{\partial^2 u}{\partial z^2}) \tag{5}$$

$$\rho\left[\frac{\partial v}{\partial t} + v\left(\frac{\partial u}{\partial x} + \frac{\partial v}{\partial y} + \frac{\partial w}{\partial z}\right)\right] = -\frac{\partial p}{\partial y} + \mu\left(\frac{\partial^2 v}{\partial x^2} + \frac{\partial^2 v}{\partial y^2} + \frac{\partial^2 v}{\partial z^2}\right) \tag{6}$$

$$\rho\left[\frac{\partial w}{\partial t} + w\left(\frac{\partial u}{\partial x} + \frac{\partial v}{\partial y} + \frac{\partial w}{\partial z}\right)\right] = -\frac{\partial p}{\partial z} + \mu\left(\frac{\partial^2 w}{\partial x^2} + \frac{\partial^2 w}{\partial y^2} + \frac{\partial^2 w}{\partial z^2}\right) \tag{7}$$

where t represents time; ρ denotes the density of water; P denotes the pressure of water; μ is the dynamic viscosity of water. The pressure p can be also decomposed into time-average

value P and the turbulent fluctuation p' as

$$p = P + p' \tag{8}$$

Substituting equations 2, 3, 4, and 8 into equations 5, 6, and 7 and taking time average give the Reynolds-averaged momentum equations

$$\begin{aligned}\rho\left[\frac{\partial U}{\partial t} + U\left(\frac{\partial U}{\partial x} + \frac{\partial V}{\partial y} + \frac{\partial W}{\partial z}\right)\right] = -\frac{\partial P}{\partial x} + \mu\left(\frac{\partial^2 U}{\partial x^2} + \frac{\partial^2 U}{\partial y^2} + \frac{\partial^2 U}{\partial z^2}\right) \\ -\rho\left[\frac{\partial}{\partial x}\left(\overline{u'u'}\right) + \frac{\partial}{\partial y}\left(\overline{u'v'}\right) + \frac{\partial}{\partial z}\left(\overline{u'w'}\right)\right]\end{aligned} \tag{9}$$

$$\begin{aligned}\rho\left[\frac{\partial V}{\partial t} + V\left(\frac{\partial U}{\partial x} + \frac{\partial V}{\partial y} + \frac{\partial W}{\partial z}\right)\right] = -\frac{\partial P}{\partial y} + \mu\left(\frac{\partial^2 V}{\partial x^2} + \frac{\partial^2 V}{\partial y^2} + \frac{\partial^2 V}{\partial z^2}\right) \\ -\rho\left[\frac{\partial}{\partial x}\left(\overline{v'u'}\right) + \frac{\partial}{\partial y}\left(\overline{v'v'}\right) + \frac{\partial}{\partial z}\left(\overline{v'w'}\right)\right]\end{aligned} \tag{10}$$

$$\begin{aligned}\rho\left[\frac{\partial W}{\partial t} + W\left(\frac{\partial U}{\partial x} + \frac{\partial V}{\partial y} + \frac{\partial W}{\partial z}\right)\right] = -\frac{\partial P}{\partial z} + \mu\left(\frac{\partial^2 W}{\partial x^2} + \frac{\partial^2 W}{\partial y^2} + \frac{\partial^2 W}{\partial z^2}\right) \\ -\rho\left[\frac{\partial}{\partial x}\left(\overline{w'u'}\right) + \frac{\partial}{\partial y}\left(\overline{w'v'}\right) + \frac{\partial}{\partial z}\left(\overline{w'w'}\right)\right]\end{aligned} \tag{11}$$

Similarly, the Reynolds-averaged continuity equation is given by

$$\frac{\partial U}{\partial x} + \frac{\partial V}{\partial y} + \frac{\partial W}{\partial z} = 0 \tag{12}$$

The Reynolds decomposition and time average give rise to correlations of turbulence fluctuation motions, which can be expressed as a stress tensor:

$$\tau_{ij} = \begin{pmatrix} \tau_{xx} & \tau_{xy} & \tau_{xz} \\ \tau_{yx} & \tau_{yy} & \tau_{yz} \\ \tau_{zx} & \tau_{zy} & \tau_{zz} \end{pmatrix} = -\rho \begin{pmatrix} \overline{u'u'} & \overline{u'v'} & \overline{u'w'} \\ \overline{v'u'} & \overline{v'v'} & \overline{v'w'} \\ \overline{w'u'} & \overline{w'v'} & \overline{w'w'} \end{pmatrix} \tag{13}$$

The nine components of this stress tensor are extra unknowns. They need to be formulated using appropriate model equations in order to close the system of partial differential equations that govern the flow field. This is the so called turbulence closure problem. For the purpose of turbulence closure, the mean flow strain rates are written as:

$$S_{xx} = \frac{1}{2}\left(\frac{\partial U}{\partial x} + \frac{\partial U}{\partial x}\right),\ S_{xy} = \frac{1}{2}\left(\frac{\partial U}{\partial y} + \frac{\partial V}{\partial x}\right),\ S_{xz} = \frac{1}{2}\left(\frac{\partial U}{\partial z} + \frac{\partial W}{\partial x}\right) \tag{14}$$

$$S_{yx} = S_{xy},\ S_{yy} = \frac{1}{2}\left(\frac{\partial V}{\partial y} + \frac{\partial V}{\partial y}\right),\ S_{yz} = \frac{1}{2}\left(\frac{\partial V}{\partial z} + \frac{\partial W}{\partial x}\right) \tag{15}$$

$$S_{zx} = S_{xz},\ S_{zy} = S_{yz},\ S_{zz} = \frac{1}{2}\left(\frac{\partial W}{\partial z} + \frac{\partial W}{\partial z}\right) \tag{16}$$

Using the the concept of the eddy viscosity (v_t), which was introduce by Boussinesq (1887), the Reynolds stress tensor (Equation 13) can be related to mean flow strain rates (equations 14, 15, and 16) as

$$\tau_{xx} = 2v_t S_{xx},\ \tau_{xy} = 2v_t S_{xy},\ \tau_{xz} = 2v_t S_{xz} \tag{17}$$

$$\tau_{yx} = 2v_t S_{yx},\ \tau_{yy} = 2v_t S_{yy},\ \tau_{yz} = 2v_t S_{yz} \tag{18}$$

$$\tau_{zx} = 2v_t S_{zx},\ \tau_{zy} = 2v_t S_{zy},\ \tau_{zz} = 2v_t S_{zz} \tag{19}$$

From Equations 1 to 19, the Reynolds-averaged Navier–Stokes equations in tensor form can be written as:

$$\frac{\partial U_j}{\partial x_j} = 0 \tag{20}$$

$$\rho\left[\frac{\partial U_i}{\partial t} + \frac{\partial}{\partial x_j}\left(U_i U_j\right)\right] = -\frac{\partial P}{\partial x_i} + \frac{\partial}{\partial x_j}\left(2\mu S_{ji} - \rho\overline{u_j' u_i'}\right) \tag{21}$$

where U_i, with $i = 1, 2, 3$, denotes the Reynolds-averaged (or mean flow) velocity component in the x_i-direction. Now, the turbulence closure problem centres at how to formulate the kinetic eddy viscosity, ν_t (or equivalently the dynamic eddy viscosity, $\mu_t = \rho\nu_t$).

3.3 The $k - \epsilon$ model

For calculations of the eddy viscosity, the $k - \epsilon$ model is the simplest and one of the most widely used turbulence models. It is a two-equation model. One of the two transport equations is written for the determination of the turbulence kinetic energy or TKE (K). The other equation is written for the determination of the TKE dissipation rate (ϵ). The combination of K and ϵ specifies the length, time and velocity scales of turbulence. There are three different kinds of $k - \epsilon$ model, namely the standard $k - \epsilon$ model, realizable $k - \epsilon$ model, and re-normalization group model (RNG). All the $k - \epsilon$ models approximate the turbulent eddy viscosity using:

$$\mu_t = \frac{\rho C_u K^2}{\varepsilon} \tag{22}$$

The standard $k - \epsilon$ model calculates TKE (K) and its dissipation rate (ϵ) from,

$$\frac{\partial}{\partial t}\left(\rho k\right) + \frac{\partial}{\partial x_i}\left(u_i \rho k\right) = \frac{\partial}{\partial x_j}\left[\left(\mu + \frac{\mu_t}{\sigma_k}\right)\frac{\partial k}{\partial x_j}\right] + G_k + G_b + S_k - \rho\epsilon \tag{23}$$

$$\frac{\partial}{\partial t}(\rho\varepsilon)+\frac{\partial}{\partial x_i}(u_i\rho\varepsilon)=\frac{\partial}{\partial x_j}\left[\left(\mu+\frac{\mu_t}{\sigma_\varepsilon}\right)\frac{\partial\varepsilon}{\partial x_j}\right]+C_{1\varepsilon}\frac{\varepsilon}{k}(G_k+C_{3\varepsilon}G_b)-C_{2\varepsilon}\frac{\varepsilon^2}{k}+S_\varepsilon \quad (24)$$

where G_b and G_k are the generation terms of turbulence kinetic energy caused by buoyancy effects and gradients of average (or mean flow) velocity, respectively. The turbulence closure constants proposed by Jones and Launder (1972), which are applicable for high Reynolds number flows, are as follows $C_{1\varepsilon}=1.44$, $C_{2\varepsilon}=1.92$, $C_{3\varepsilon}=-0.33$, $C_\mu=0.09$, $\sigma_k=1$ and $\sigma_\epsilon=1.3$

The $k-\epsilon$ model gives the best results in flow regions with high Reynolds number. Therefore, it has a limitation in solving flows in near-wall regions since the Reynolds number is usually low.

3.4 The $k-\omega$ model

The URANS $k-\omega$, which is generally classified into two types, the standard $k-\omega$ model and the shear stress transport (SST) model, is a two-equation model, first developed by Wilcox (1993). It uses the same approach as $k-\epsilon$ to find K, but instead of using turbulent energy dissipation ϵ, it uses the so-called specific dissipation rate, ω. The $k-\epsilon$ model is known to have shortcomings in modeling low Reynolds number. The $k-\omega$ can be used in near-wall regions where the Reynolds number is very low, and K tends to be zero because of non-slippery conditions on the wall surface. The K and ω are computed from:

$$\frac{\partial}{\partial t}(\rho k)+\frac{\partial}{\partial x_i}(u_i\rho k)=\frac{\partial}{\partial x_j}\left[\left(\mu+\frac{\mu_t}{\sigma_k}\right)\frac{\partial k}{\partial x_j}\right]+G_k+S_k \quad (25)$$

$$\frac{\partial}{\partial t}(\rho\omega)+\frac{\partial}{\partial x_i}(u_i\rho\omega)=\frac{\partial}{\partial x_j}\left[\left(\mu+\frac{\mu_t}{\sigma_\omega}\right)\frac{\partial\omega}{\partial x_j}\right]+G_\omega+S_\omega \quad (26)$$

where G_k is the generation of TKE that arises due to mean velocity gradients; G_ω is the generation of specific dissipation rate due to the mean velocity; S_ω is the modulus of the mean rate of strain tensor of ω. The constants σ_k and σ_ω were chosen to be 0.5 as stated in Wilcox (1993). The turbulent eddy viscosity in this model is calculated by:

$$v_t = \frac{k}{\omega} \tag{27}$$

3.5 The SST $k-\omega$ turbulence model

The URANS SST $k-\omega$ model is a two-equation turbulence model that was introduced by Menter (1994). It is based on the $k-\omega$ model and a transformed $k-\epsilon$ model. The main difference between this model and a standard $k-\omega$ model is how the model calculates the turbulent eddy viscosity to account for the transport of the principle turbulent shear stress. It effectively uses the mix of the $k-\omega$ model in the near-wall region with the free-stream independence of the $k-\epsilon$ model in flow regions far from the walls. Therefore, it reduces the computational demands (Stahlmann (2014)). The equation of K is the same as the standard $k-\omega$ model, but the equation of ω is slightly different and is given by:

$$\frac{\partial}{\partial t}(\rho\omega) + \frac{\partial}{\partial x_i}(u_i\rho\omega) = \frac{\partial}{\partial x_j}\left[\left(\mu + \frac{\mu_t}{\sigma_\omega}\right)\frac{\partial\omega}{\partial x_j}\right] + G_\omega + S_\omega + D_\omega \tag{28}$$

where D_ω is a cross diffusion term that blends the standard $k-\epsilon$ model and the standard $k-\omega$ model.

3.6 Model channel and boundary conditions

The computational model channel is shown in Figure 3.1. The model channel had six boundaries: 1) one later open inlet at upstream; 2) one later open outlet at downstream; 3)

Table 3.1: Geometric elements of the computational model channel in this study

Parameter	Value	Unit
Pier diameter (D)	10	cm
Cylinder height	50	cm
Channel length downstream of the pier centre	110	cm
Channel length upstream of the pier centre	40	cm
Channel width on both sides of the pier centre	30	cm

one flat solid bed; 4) one horizontal opening at the top; 5) two parallel solid sidewalls. A cylinder (or a circular pier) of diameter $D = 10$ cm was placed vertically from the solid bed to the top opening. The cylinder was fitted with a splitter plate of 0.2 cm thick on either the upstream side or the downstream side. In the x-direction, the longitudinal length of the plat ranged from $0.5D$ to $1D$. In the z-direction (or the lateral direction), the model channel had a width of $6D$ between the two parallel sidewalls. The cylinder was located in the middle of the channel. Therefore, the flow width between the channel sidewall and cylinder's side surface was equal to $2.5D$. The sidewalls were far enough from the cylinder, to avoid significant effects of the artificial sidewalls on the flow characteristics around the cylinder. The model channel had a total longitudinal length of $15D$; the lengths were $3.5D$ and $10.5D$ upstream and downstream of the cylinder, respectively. The downstream length was large enough to allow the development of turbulent eddies and flow patterns, which are of interest in this study. The upstream length accommodated the development of inlet flow approaching the cylinder. Furthermore, a UDF function was used at the inlet to get a fully developed flow before cylinder. In the y-direction (or the vertical direction), the channel dimension was $5D$. This choice was made to have a similar cylinder condition to Dai et al. (2018). Nevertheless, the focus of this study was on the near-bed flow characteristics. The geometric elements of the model channel are summarised in Table 3.1.

A structured prism mesh with a triangular base was generated around the cylinder (Figure 3.3) and near-bed level (Figure 3.5) to get accurate result at those regions. This kind of mesh has six nodes. A structured mesh contains much more elements than an unstructured

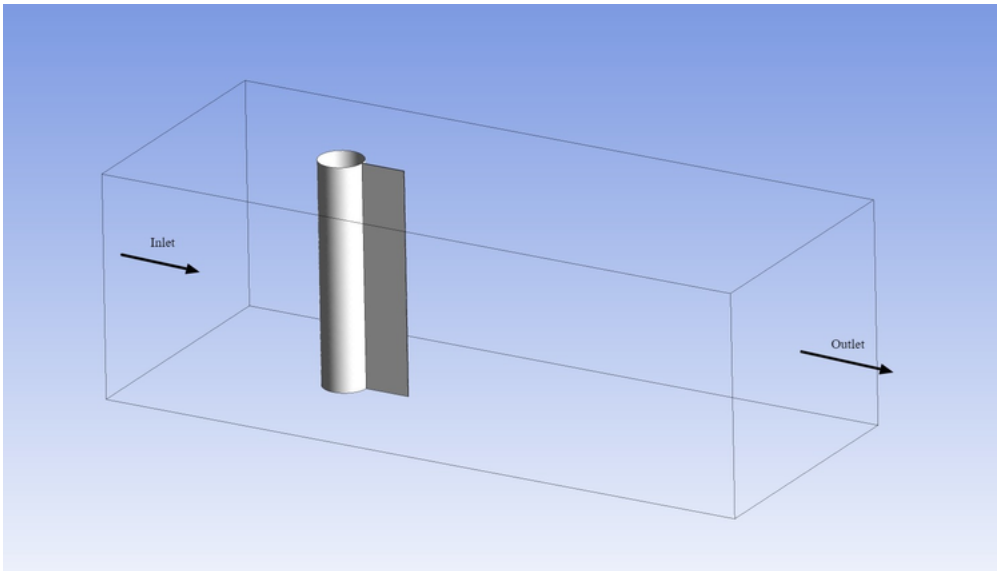

Figure 3.1: Geometry of the computational model channel for simulation of flow around a cylinder fitted with a splitter plate on the downstream side.

mesh. As we are more interested in regions near the cylinder and close to the bed level, and to prevent high computational cost, a simple tetrahedron mesh with four nodes was generated using the Ansys meshing software to cover the remaining computational model channel (Figure 3.1). The mesh generation used a cell size of 0.5 cm for some CFD runs and 1 cm for other runs. The mesh with 1-cm cell size had about four million cells. The regions near the cylinder and bed level were of particular interest. Therefore, inflation layers were used in these regions to obtain fine cell resolutions and hence to capture boundary layer flow characteristics. Various views of the tetrahedron mesh used in this study are shown in Figures 3.2 and 3.4. A close-up view of the inflation layers near the bed level and around the cylinder is provided in Figures 3.3 and 3.5. The average mesh quality parameters for C1—C6 were as follows: aspect ratio for all the cells was equal to 2.57. The skewness was equal to 0.2. The element quality and orthogonal quality was 0.78 and 0.79, respectively. All the parameters of mesh quality were in the excellent range.

The following conditions were imposed at the model channel boundaries:

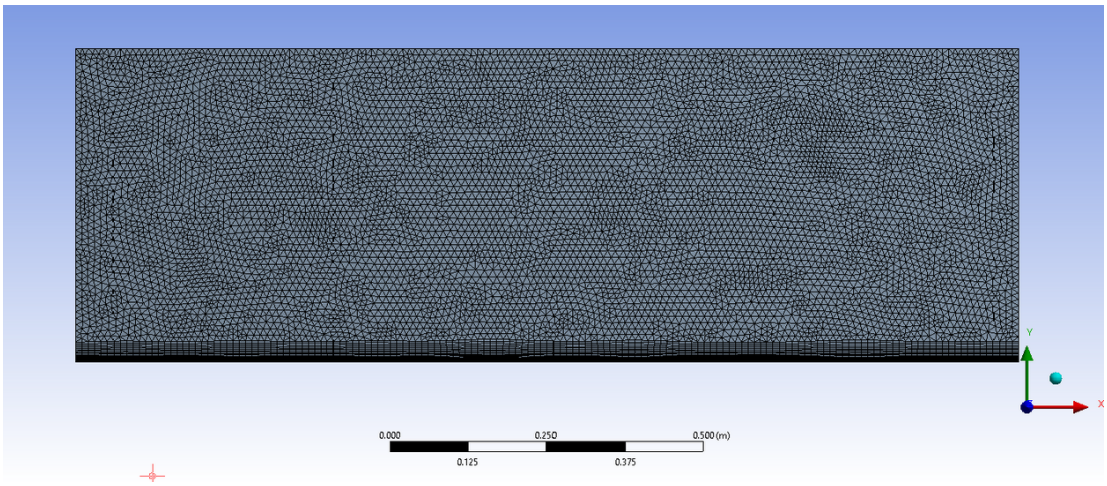

Figure 3.2: Side view of the mesh showing inflation layers near the channel-bed.

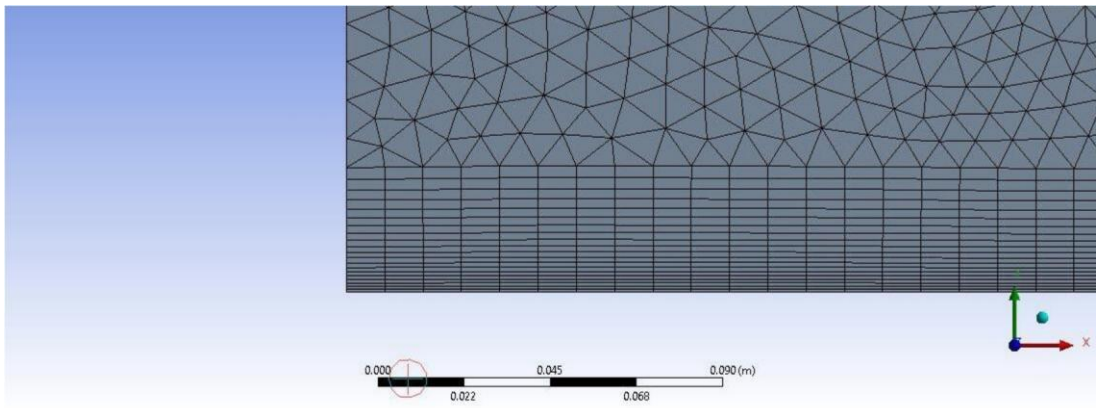

Figure 3.3: Close-up view of the mesh showing inflation layers near the channel-bed.

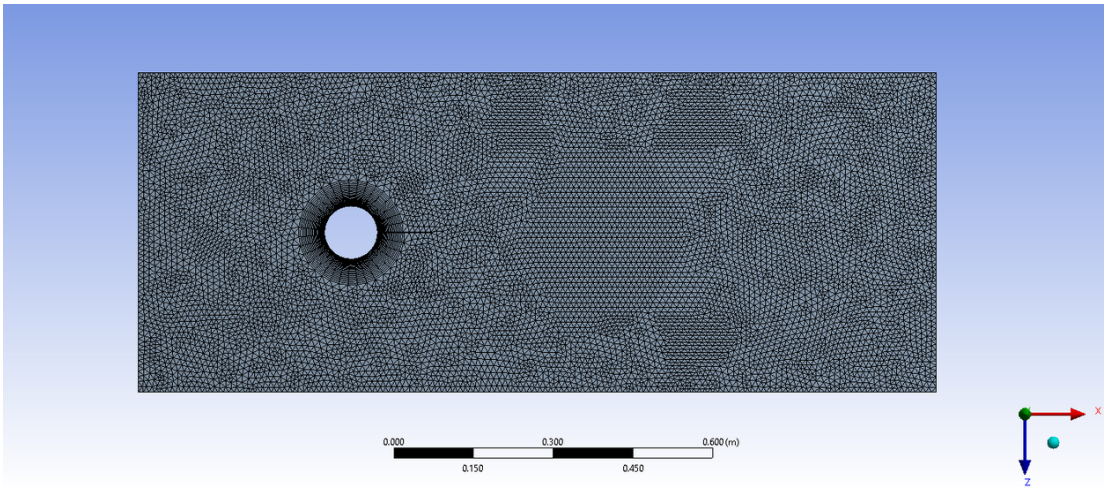

Figure 3.4: Top view of the mesh showing inflation layers around the cylinder.

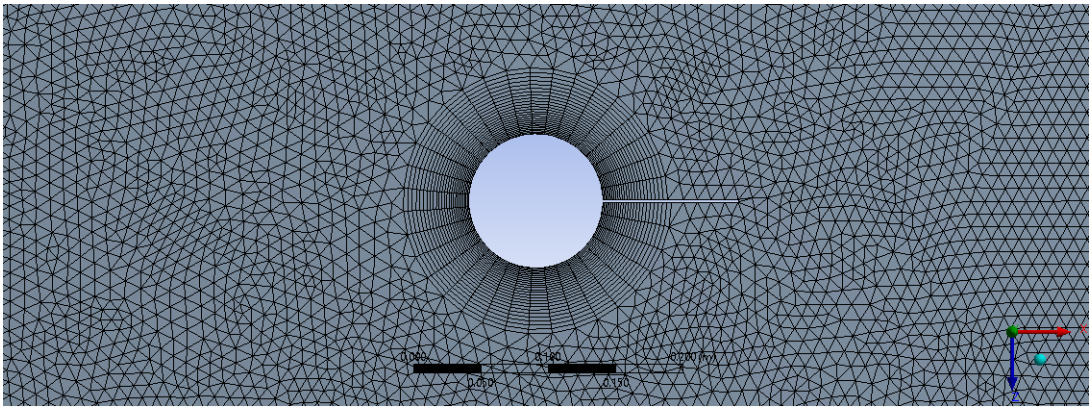

Figure 3.5: Close-up view of inflation layers around the cylinder.

- At the upstream inlet, a user defined function (UDF) was used to prescribe the velocity component U in the x-direction. The vertical profile of U followed the 1/7th power law for turbulent velocity distribution (De Chant (2005)). The velocity components V and W in the vertical and lateral directions were set to zero. This means that the inlet velocity was normal to the boundary. U was zero at the channel bed (non-slippery condition), increased with vertical distance, and reached the maximum velocity of 1.8 m/s at the water surface (or at $y = \delta$), where δ is the thickness of boundary layer. The turbulence intensity was set to 5% of the mean flow.

- At the downstream outlet, the pressure was set to zero.

- At the channel-bed, non-slippery boundary conditions were applied (or $U = V = W = 0$)

- On the top and two parallel sidewalls, free-slippery boundary conditions were applied. This means that shear stresses in all three directions were set to be zero.

No-slip boundary conditions were also applied at the cylinder surface.

3.7 Simulations

This study aims to determine the optimal value for the splitter plate length, L, for reducing turbulence, which is known to be responsible for scour around bridge piers. For this purpose, ten runs (Table 3.2 were performed. Runs T1 – T4 were test runs that were intended to demonstrate the independence of numerical results on mesh configuration (spatial resolution), time step ΔT, and the choice of turbulence closure models. Run C1 simulated turbulent flow around a bare cylinder as the base case. Runs C2 – C4 simulated the effects of splitter plates of different lengths L, fitted on the downstream side of the cylinder, on the

Table 3.2: A summary of conditions for ten numerical simulations.

Run ID	L/D	Plate position	Mesh size (mm)	Δ T (s)	Turbulence model	Node	Element
T1	0.5	Downstream	5	0.0025	SST k-ω	1671200	7836245
T2	0.5	Downstream	10	0.00125	SST k-ω	848957	3980770
T3	0.5	Downstream	10	0.0025	k-ϵ	848957	3980770
T4	0.5	Downstream	10	0.0025	k-ω	848957	3980770
C1	0	Absent	10	0.0025	SST k-ω	857614	4002085
C2	0.5	Downstream	10	0.0025	SST k-ω	848957	3980770
C3	0.6	Downstream	10	0.0025	SST k-ω	852479	3983780
C4	1.0	Downstream	10	0.0025	SST k-ω	851118	3982153
C5	0.5	Upstream	10	0.0025	SST k-ω	854212	3989147
C6	1.0	Upstream	10	0.0025	SST k-ω	849160	3978663

flow. Runs C5 and C6 simulated the effects of splitter plates fitted on the upstream side of the cylinder.

Table 3.2 lists the conditions of the ten runs. For all the runs, the convergence criterion was set to 10^{-6} at each time step during the integration over time. On the basis of the maximum longitudinal velocity (1.8 m/s) at the velocity inlet (Figure 3.1), the flow depth (0.5 m) (Table 3.2), and the kinetic viscosity of water ($\nu = 1 \times 10^{-6}$ m/s^2), the Reynolds number has a value of $Re_D = 1.8 \times 10^5$. This Re value is sufficiently high to ensure fully turbulent flow around the cylinder, which reflects the nature of turbulent flows in river channels. The conditions of Runs C3 and C4 listed in Table 3.2 match those of Dai et al. (2018), which allows a comparison of data from our study and theirs. To our best knowledge, Dai et al. (2018) is the only study reported in the literature, which addressed the issue of vortex shedding suppression using a splitter plate in 3-D turbulent flow.

Chapter 4

Results and discussions

4.1 Sensitivity test

Runs T1 and C2 (Table 3.2) used the same simulation conditions, except the mesh size. The mesh size was 5 mm for T1 and 10 mm for C2. Values of the longitudinal velocity U were extracted from the model results for these two runs at the model time of $t = 2$ s, for ten selected x locations along each of the nine lines shown in Figure 4.1. The ten x locations are listed in Table 4.1. For each of the ten x locations, the U values at the nine z coordinates on the red lines in Figure 4.1 were averaged. The averages are compared in Table 4.1. The relative difference, ΔU_1, of the average values between the two runs is smaller than 5%. The mesh for Run T1 consisted of almost two times the nodes of the mesh for Run C2 and thus incurred much higher computing costs. It is desirable to use the C2 mesh with a spatial resolution of 10 mm. Note that the C2 mesh allowed for the same inflation layers to resolve near-wall regions as the T1 mesh.

The conditions for Runs T2 and C2 differed only in time step ΔT. ΔT was 0.00125 s for T2 and 0.0025 s for C2. The average velocities are compared in Table 4.1 between Runs T2 and C2, in the same way as the comparison of the average velocities between Runs T1 and C2 in the table. For most of the x locations, the relative difference, ΔU_2, of

the corresponding average velocities between the two runs are smaller than 5%. For only one location ($x = 0.5$), the relative difference is 6.9%. It is acceptable to use the time step of $\Delta T = 0.0025$ s.

Runs T3, T4 and C2 differed in the choice of turbulence closure models. The k-ϵ model, the k-ω model and the SST k-ω model were used for turbulence closure for the three runs, respectively. The average velocities were compared in Table 4.1. The relative differences, $\triangle U_3$, between T3 and C2, and $\triangle U_4$, between T4 and C2 are also small. Relatively speaking, the SST k-ω model is known to give a better performance in simulations of complicated turbulent flow. For this reason and on the basis of comparison, the SST k-ω model was used in subsequent runs in this study.

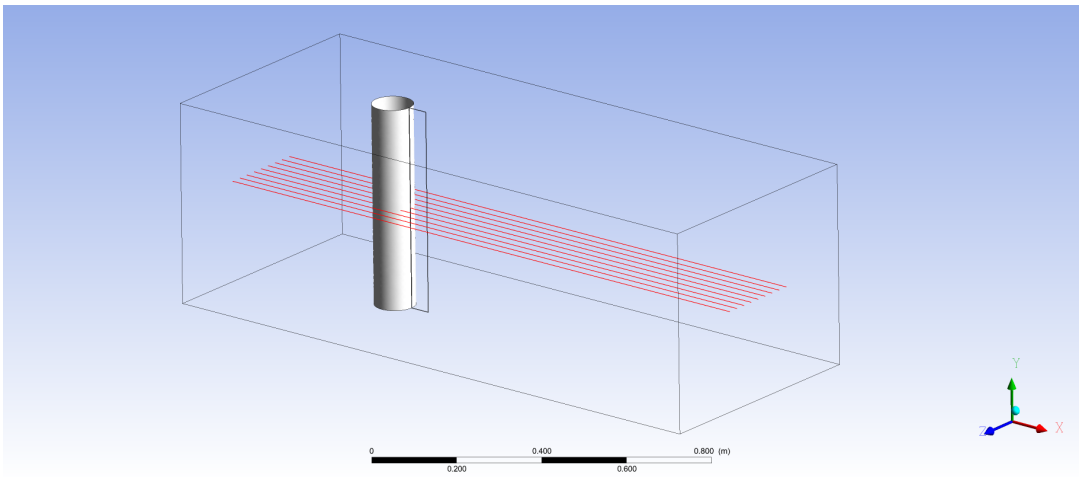

Figure 4.1: Middle-depth lines at nine selected z locations where values of velocity U were compared among Runs T1 – T4 and C2. The vertical coordinates of the lines are $y = 25$ cm (or the middle depth).

4.2 Drag and lift coefficients

In order to validate the CFD results from this study, values of the averaged drag coefficient $\overline{C}_D$ and the fluctuating lift coefficient C'_L were compared with the numerical results

Table 4.1: Comparison of average velocities at ten selected x locations among Runs T1 – T4 and C2. The model time of the velocities was $t = 2$ s.

Points	X (m)	Average velocity (m/s)					Relative difference (%)			
		C2	T1	T2	T3	T4	$\triangle U_1$	$\triangle U_2$	$\triangle U_3$	$\triangle U_4$
1	0	1.8	1.8	1.8	1.8	1.8	0	0	0	0
2	0.17	1.77	1.75	1.77	1.77	1.77	1.1	0	0	0
3	0.33	1.67	1.63	1.7	1.65	1.64	2.4	1.8	1.2	1.5
4	0.5	1.3	1.35	1.44	1.51	1.6	3.9	6.9	16.5	2.3
5	0.67	1.48	1.55	1.43	1.64	1.58	4.7	3.4	10.7	6.8
6	0.83	1.58	1.64	1.52	1.72	1.79	3.8	3.8	8.6	1.3
7	1	1.63	1.66	1.6	1.73	1.78	1.8	1.8	6.1	9.2
8	1.17	1.66	1.68	1.69	1.73	1.8	1.2	1.8	4	8.4
9	1.33	1.63	1.7	1.7	1.72	1.78	4.3	4.3	5.8	9.2
10	1.5	1.66	1.68	1.72	1.7	1.79	1.2	3.6	3.8	7.8

from another independent study by Dai et al. (2018). The values of C_D (Equation 29) and C_L (Equation 30) varied from time step to time step. In this study, the C_D values were averaged over the simulation time period and over the length of the cylinder.

$$C_D = \frac{2F_D}{\rho A U^2} \tag{29}$$

$$C_L = \frac{2F_L}{\rho A U^2} \tag{30}$$

where F_D is the drag force in the direction of flow; F_L is the lift force normal to the flow direction; ρ is the density of the fluid which is 1000 kg/m^3 in this study; U is the depth-averaged speed of flow approaching the cylinder and A is the projected frontal area of the cylinder, which is the height times to diameter of the cylinder HD. F_D and F_L are defined as:

$$F_D = \int_A dF_D = \int_A P_x cos\theta dA \tag{31}$$

$$F_L = \int_A dF_L = \int_A P_z cos\theta dA \tag{32}$$

where P_x is the local pressure in the x-direction; P_z is the local pressure in the z-direction; θ is the angle between the cylinder and the flow. Since the flow is normal to the cylinder, $\theta = 0$ and $cos\theta = 1$.

The C_l' was obtained by taking the root mean square (RMS) (Equation 33) of all the C_L values over the entire simulation period. The reason behind using C_l' instead of $\overline{C}_L$ is that some C_L values were negative. Statistically, we are interested in the magnitude of C_L, therefore, take the RMS of all the C_L values. This treatment avoids negative C_L values. The results of ($\overline{C}_D$) and (C_l') are shown in Table 4.2.

$$RMS_{C_L} = \sqrt{\frac{C_{L1}^2 + C_{L2}^2 + \ldots + C_{LN}^2}{N}} \tag{33}$$

The $\overline{C}_D$ and C_l' values for Case 1 (Table 3.2) were 0.888 and 0.638, respectively. This is consistent with the results of Dai et al. (2018). They reported the $\overline{C}_D$ and C_l' values to be 0.897 and 0.644, respectively. To further validate the $\overline{C}_D$ and C_l' values from this study, Case 3 (Table 3.2) was modelled for a comparison with the results of Dai et al. (2018). The values of $\overline{C}_D$ and C_l' for Case 3 from this study were 0.687 and 0.142, respectively, compared with 0.644 and 0.176 from Dai et al. (2018). To our best knowledge, Dai et al. (2018) is the only study that used the same Reynolds number and tail length. The best agreement in terms of $\overline{C}_D$ values is for Cases 5 and 6. Both Cases 5 and 6 reduced $\overline{C}_D$ values by 45%, compared to the $\overline{C}_D$ value for Case 1. For Cases 4, 3 and 2 (Table 3.2), the $\overline{C}_D$ values reduced by 24.5%, 22.6% and 21.15%, respectively. This study showed that a tail fitted at the upstream side of the cylinder is more capable of reducing $\overline{C}_D$ values than a tail fitted at the downstream side of the cylinder. This is consistent with the finding of Qiu, Sun, Wu, and Tamura (2014). They reported that at Reynolds numbers in the range of

Table 4.2: Force coefficients and their reduction by using upstream and downstream splitter plate

Cases (Table 3.2)	*1*	2	3	4	5	6
$\overline{C}_D$	0.889	0.7	0.687	0.669	0.482	0.49
Reduction (%)	-	21.15	22.6	24.5	45.65	44.8
C_l'	0.638	0.132	0.142	0.116	0.195	0.182
Reduction (%)	-	79.3	77.78	81.87	69.41	71.45
C_D (Dai et al. (2018))	0.897	-	0.634	-	-	-
C_l' (Dai et al. (2018))	0.644	-	0.176	-	-	-

$6.9 * 10^4$ to $8.28 * 10^5$, a tail fitted at the upstream side of the cylinder was more capable in diminishing $\overline{C}_D$, in comparison to the cylinders fitted with a tail at the downstream side.

In terms of C_l', the maximum reduction was achieved for Case 4. The reduction was almost 82% compared to Case 1. Good reductions were also achieved for Cases 2 and 3. The reductions were 77.78% and 79.3%, respectively. Cases 5 and 6 gave reductions of 69.41% and 71.45% of C_l', respectively. Designs of in-stream hydraulic engineering structures, engineers should pay more attention to C_l' than $\overline{C}_D$. The fluctuating lift coefficient is of greater importance because the lift forces cause vibrations on the structures and increase vortex shedding power. Overall, the value of C_l' should be considered as the most important parameter and therefore Case 4 is recommended.

4.3 Turbulence Kinetic Energy (TKE)

One of the most important parameters causing degradation the riverbed is the existence of high TKE near the bed level. In order to reduce scour depth, we have to reduce TKE close to the bed level. To improve the accuracy of TKE calculations, the TKE contours at a vertical distance of 2 cm above the bed level were investigated instead of the TKE at the bed level. The TKE contours are plotted in Figures 4.2 to 4.7 for assessment of Cases 2 to 6 in terms of reduction of TKE.

From Figure 4.2, it is clear that there was a region of high TKE values immediately

downstream of the cylinder for Case 1 (Table 3.2). Figures 4.3 to 4.7 show horizontal planes of TKE, where high TKE regions were visible. In Figure 4.3, there were two regions of high TKE values (red color regions). Interactions between the low-pressure region behind the cylinder with high-pressure region from the sides of the cylinder created powerful vortices. As a result, the TKE increased. These high magnitudes of TKE removed the sediments in flow direction and transported them to downstream. Figure 2.4b shows the experimental results of scouring downstream of the circular cylinder. From the scouring regions of sediments in Figure 2.4b, one can notice that these regions were the areas of high TKE (Figure 4.3).

Figures 4.4 and 4.5 show the TKE contours for Cases 2 and 4, respectively. The contours show a region of weaker TKE on the downstream side of the cylinder, compared to Case 1. Adding a plate can significantly suppress vortices and reduce TKE in the wake of the cylinder. Case 5 (Figure 4.6) gave a weaker performance in comparison to Cases 2 and 4. Case 6 (Figure 4.7) gave some improvement in terms of TKE reduction. For quantification of TKE values, the average of TKE values at 9 Z locations (Figure 4.8) was calculated. The results are plotted in (Figure 4.9).

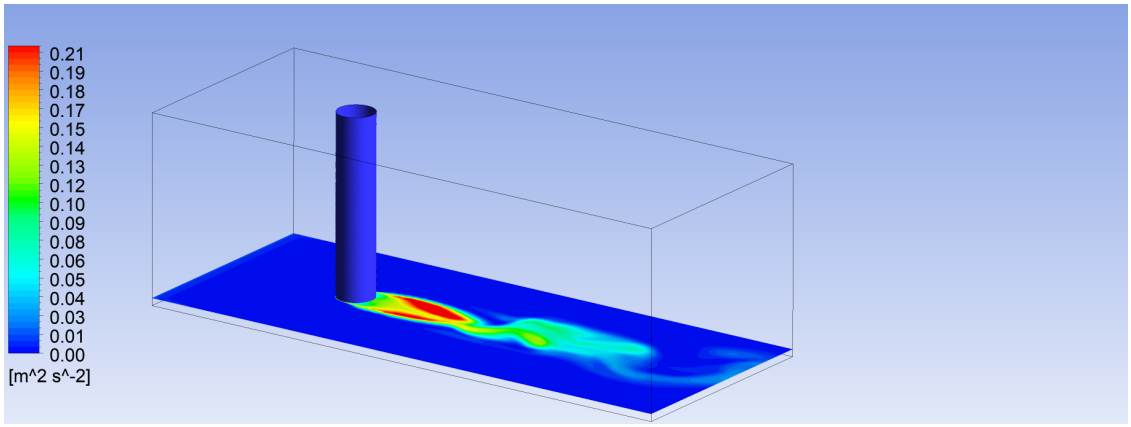

Figure 4.2: 3D view of TKE contour in the 2cm distance of Case 1

Figure 4.9 shows the average TKE values at a vertical distance of 2 cm from the bed

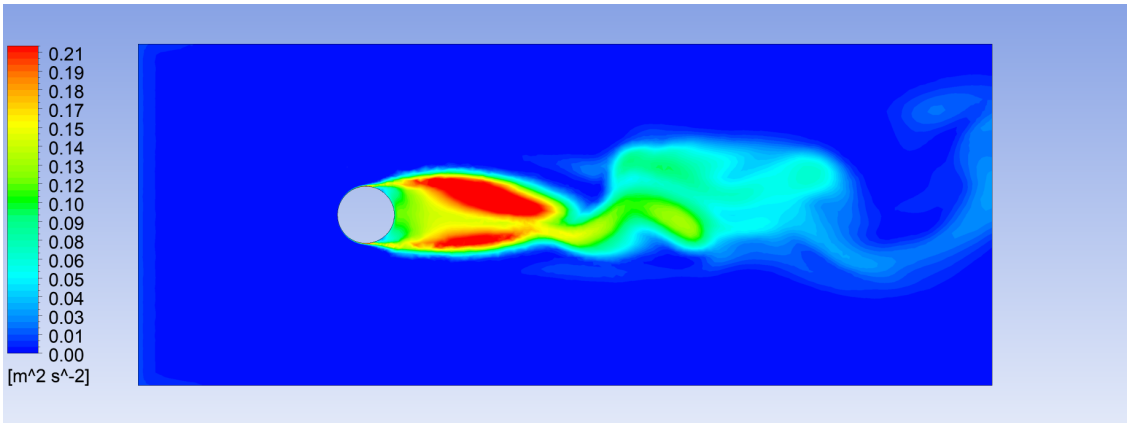

Figure 4.3: TKE contours in the horizontal plane at a vertical distance of 2 cm from the river bed for Case 1

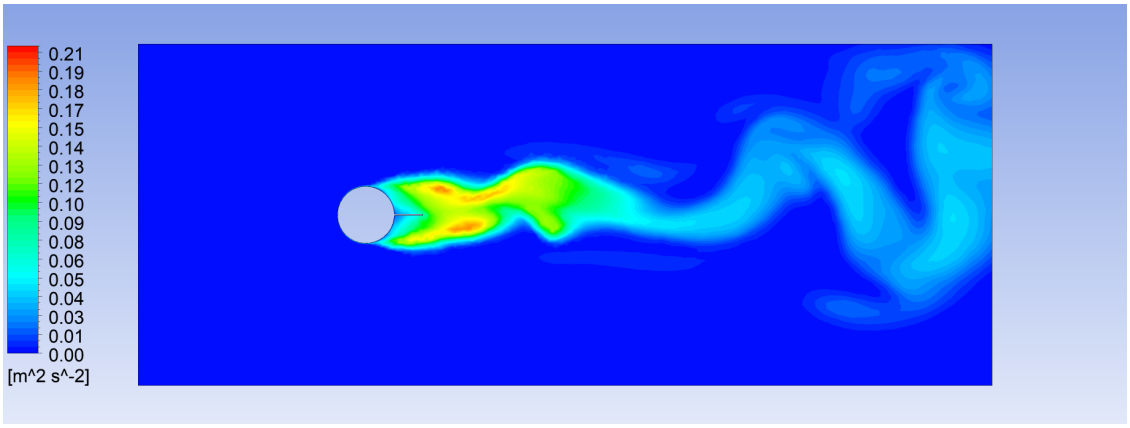

Figure 4.4: TKE contours in the horizontal plane at a vertical distance of 2 cm from the river bed for Case 2

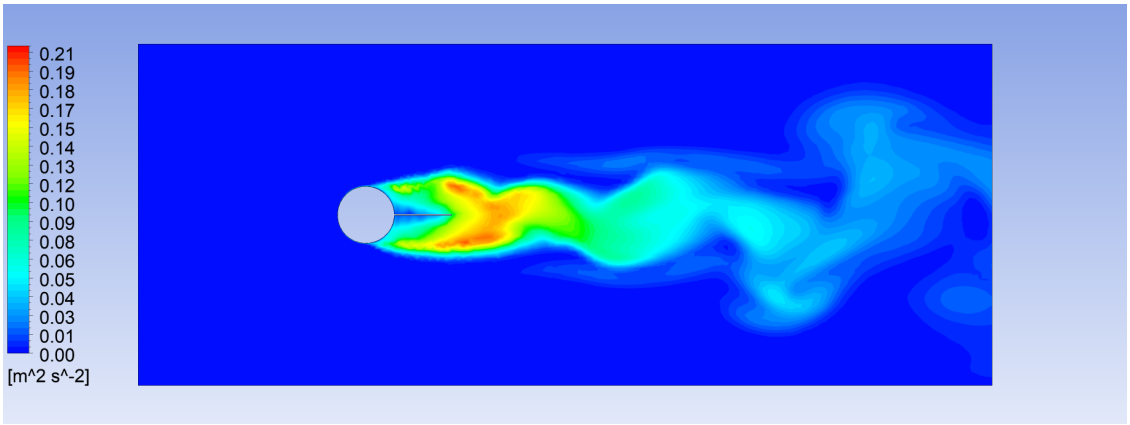

Figure 4.5: TKE contours in the horizontal plane at a vertical distance of 2 cm from the river bed for Case 4

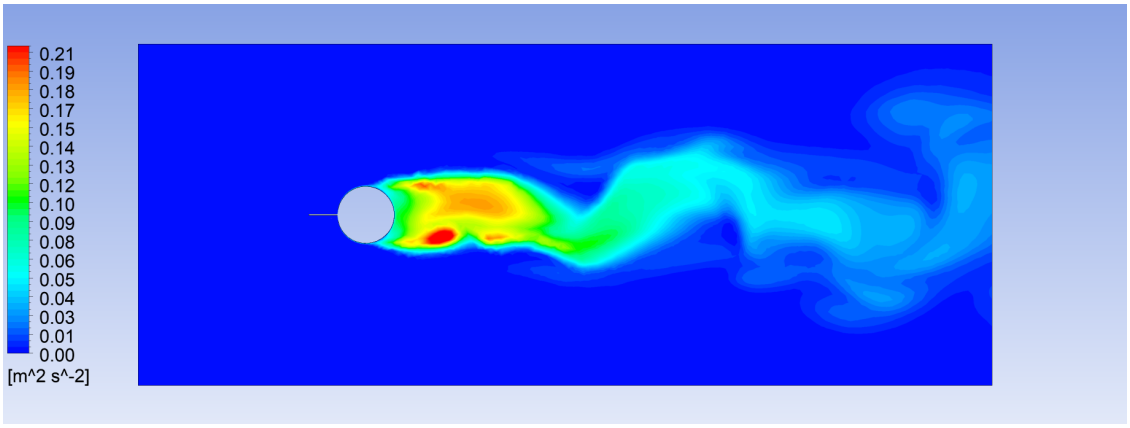

Figure 4.6: TKE contours in the horizontal plane at a vertical distance of 2 cm from the river bed for Case 5

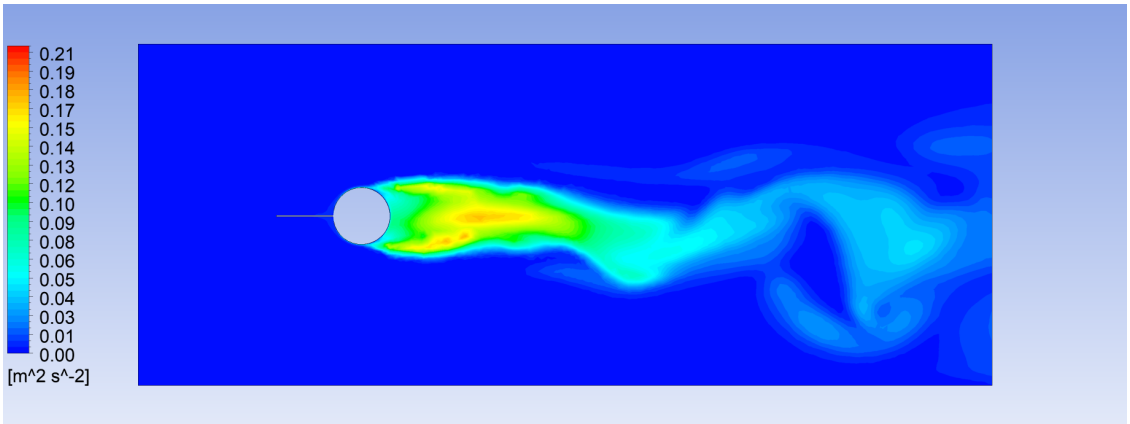

Figure 4.7: TKE contours in the horizontal plane at a vertical distance of 2 cm from the river bed for Case 6

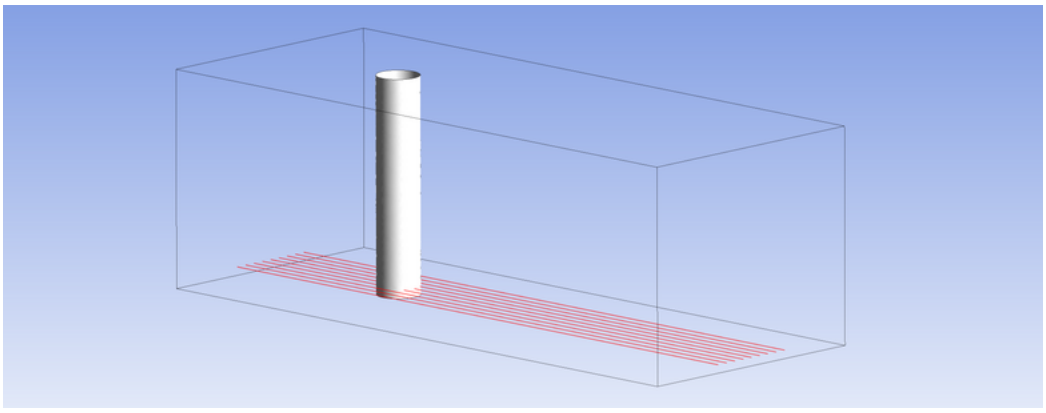

Figure 4.8: 9 lines located at 2 cm from the bed

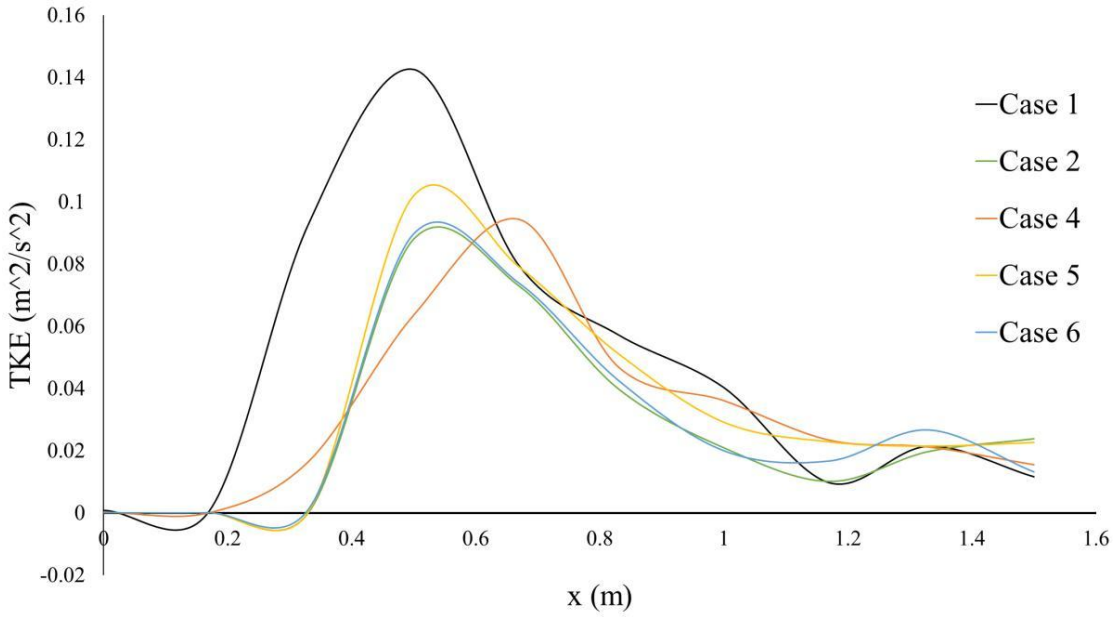

Figure 4.9: Distributions of average TKE values at a vertical distance of 2 cm from the bed. The bridge pier is located at $x = 0.35 - 0.45$ m

level. Case 1 (the black curve) produced a peak TKE of 0.142 m^2/s^2. Case 5 reduced the peak TKE to 0.12 m^2/s^2. This is a 14% reduction in the peak value of TKE. Cases 2, 4 and 6 decreased the peak value of TKE to about 0.087 m^2/s^2 that is equal to 38.7% reduction in peak TKE value. Case 4 led to a shift of the location of peak TKE value towards downstream and a gradual variations of TKE values around the peak. De Araujo et al. (2018) and Ozkan et al. (2017) demonstrated that when the $L/D = 1$ the vortex formation shifted location towards downstream of the cylinder. Since the formation of vortices increases the TKE, therefore, the results from this study are consistent with those of De Araujo et al. (2018) and Ozkan et al. (2017).

4.4 Bed shear stress

There are four different methods of calculating bed shear stress: 1) Depth-averaged flow method; 2) Eddy viscosity method; 3) The law of the wall method; 4) Reynolds shear stress method. In this study, the eddy viscosity and Reynolds shear stress at the bed level were investigated. These two parameters are a significant quantity for determining scour, in addition to TKE. Regions of high shear stress are more likely to experience scouring. Let u^* denote the friction velocity. The bed shear stress is given by:

$$\tau_b = \rho \, u^* \tag{34}$$

Contours of the bed shear stress for Cases 1, 2, 4, 5 and 6 are shown in Figures 4.10 to 4.14. Just downstream of the cylinder where the velocities had very low magnitude and some of them were in the negative direction (towards upstream), the blue region shows zero or negative bed shear stresses. This means that the shear stresses were in the direction towards the upstream side because the vortices in the wake of the cylinder generated flow reversal.

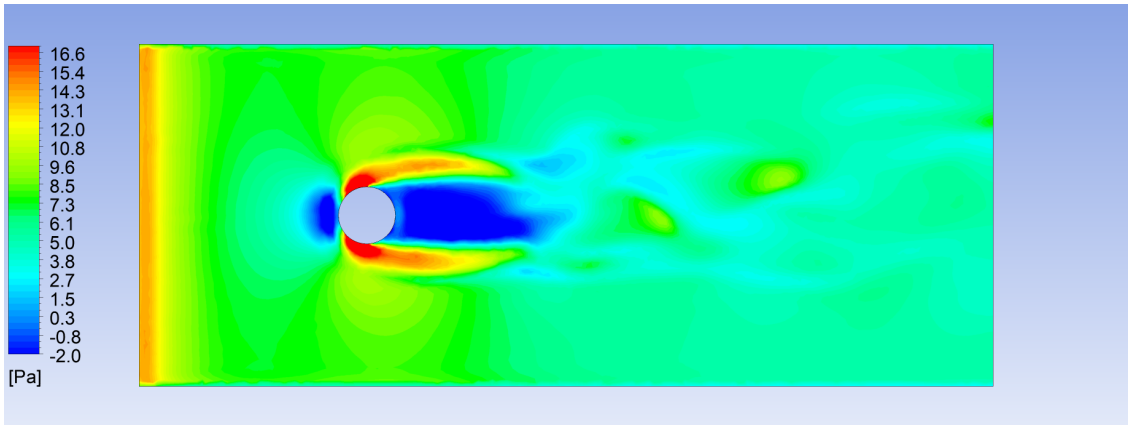

Figure 4.10: Bed shear stress contours for Case 1

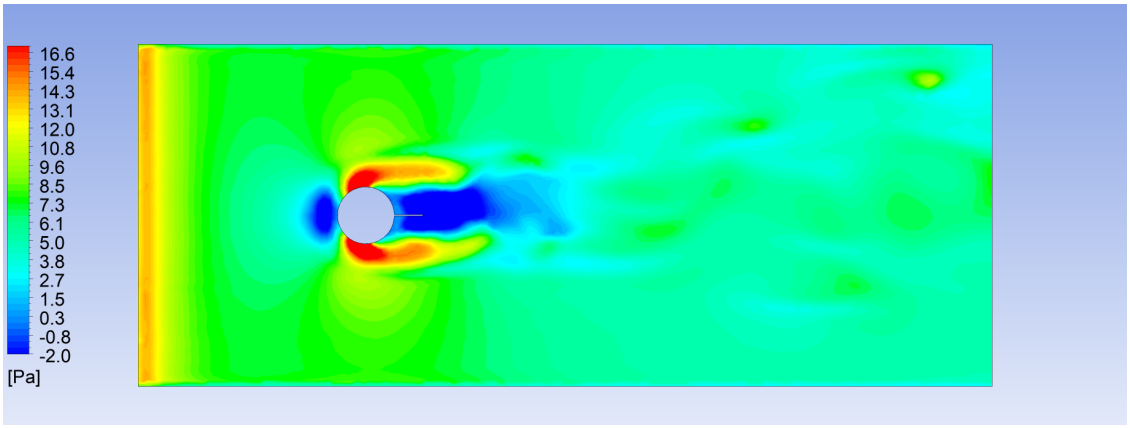

Figure 4.11: Bed shear stress contours for Case 2

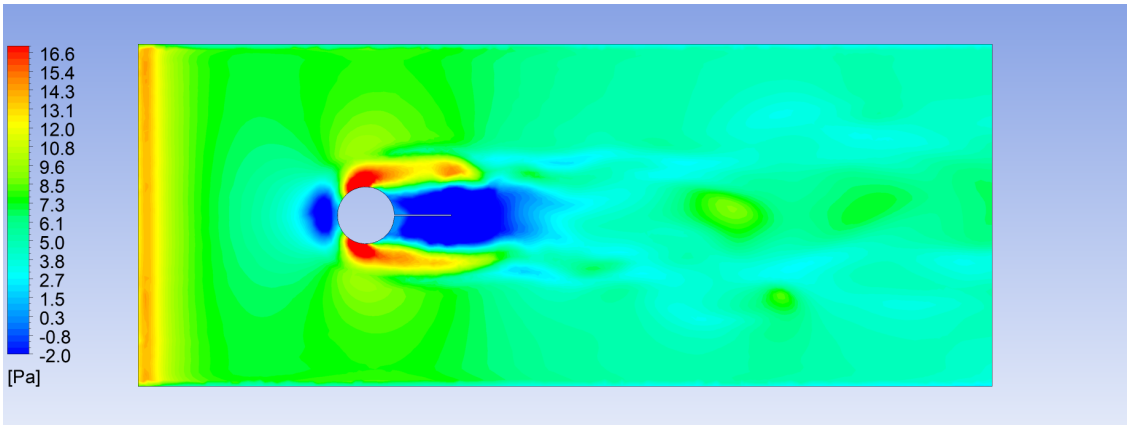

Figure 4.12: Bed shear stress contours for Case 4

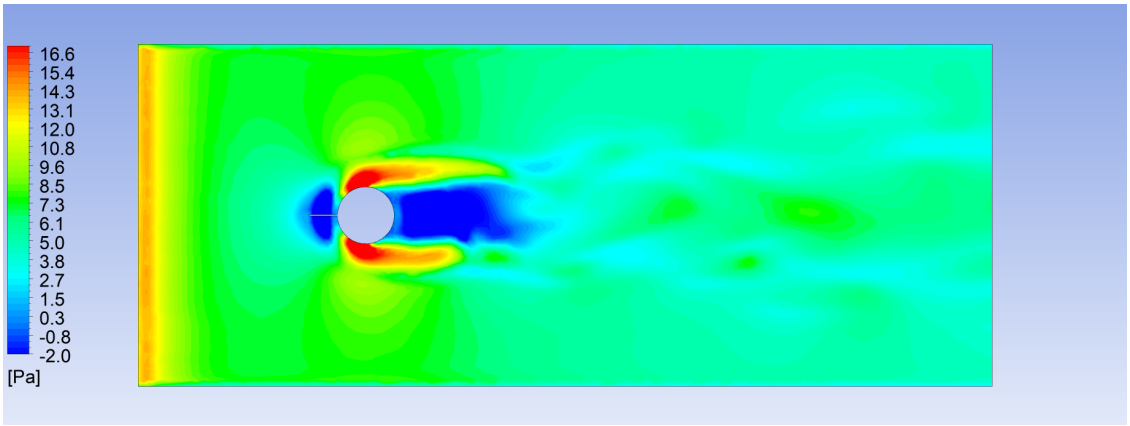

Figure 4.13: Bed shear stress contours for Case 5

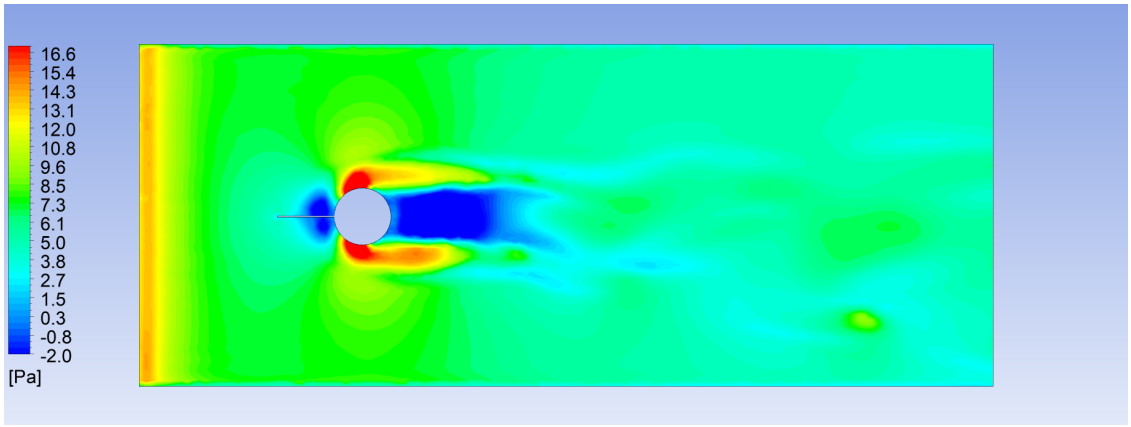

Figure 4.14: Bed shear stress contours for Case 6

Figures (4.11–4.13) are snapshots from the last time step of the simulation. We modeled C4 for more than 5 seconds to recognize if there is any difference in the snapshots. Figure 4.15 shows C4 after 6s of simulation. Comparing Figure 4.15 to 4.12 shows the minimal differences in high bed shear stress regions. Therefore, the contours after 5s of the simulation are approximately the same.

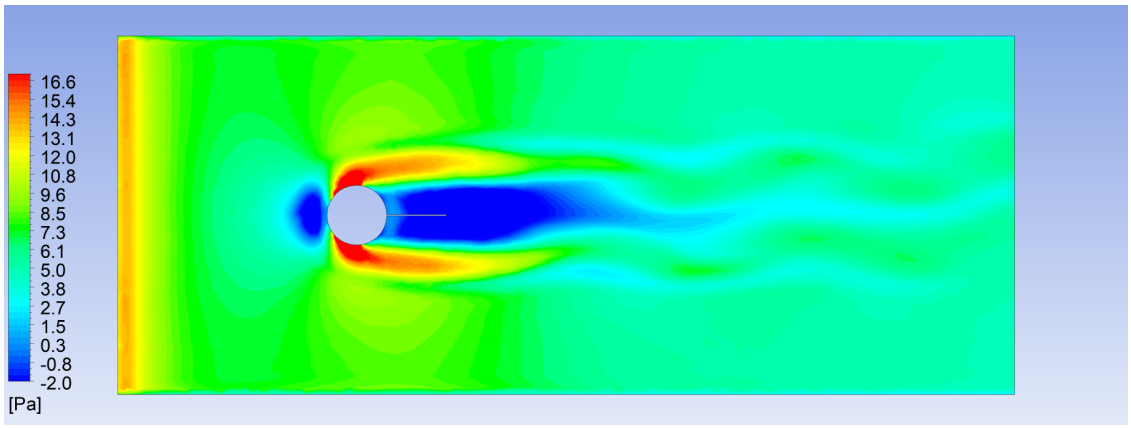

Figure 4.15: Bed shear stress contours for C4 at 6s of simulation

The values of the bed shear stress at 9 selected z locations (Figure 4.16) are analyzed in detail. The 9 z locations evenly spaced. The results are plotted in Figure 4.17.

In Figure 4.17, the black curve is the averaged (over the 9 z locations) bed shear stress

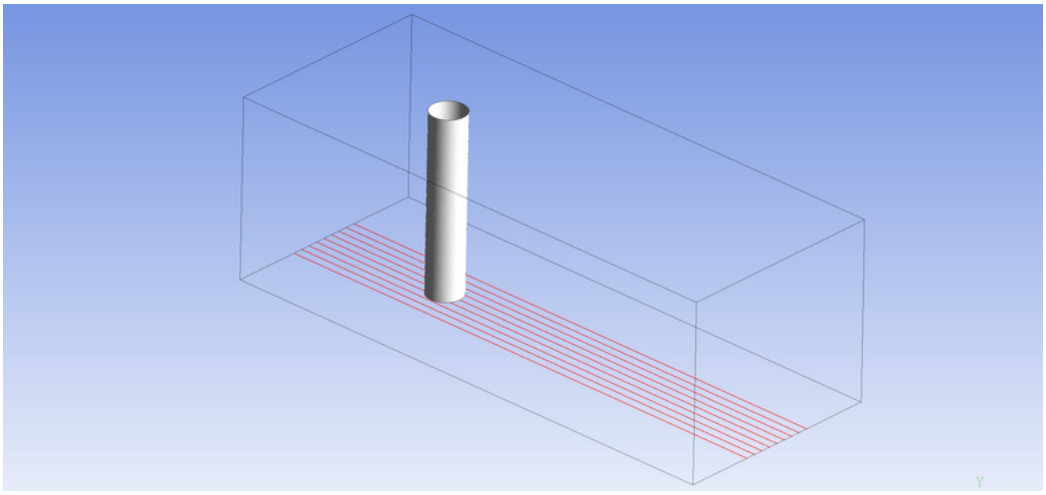

Figure 4.16: The 9 selected z locations where the bed shear stress values were discussed

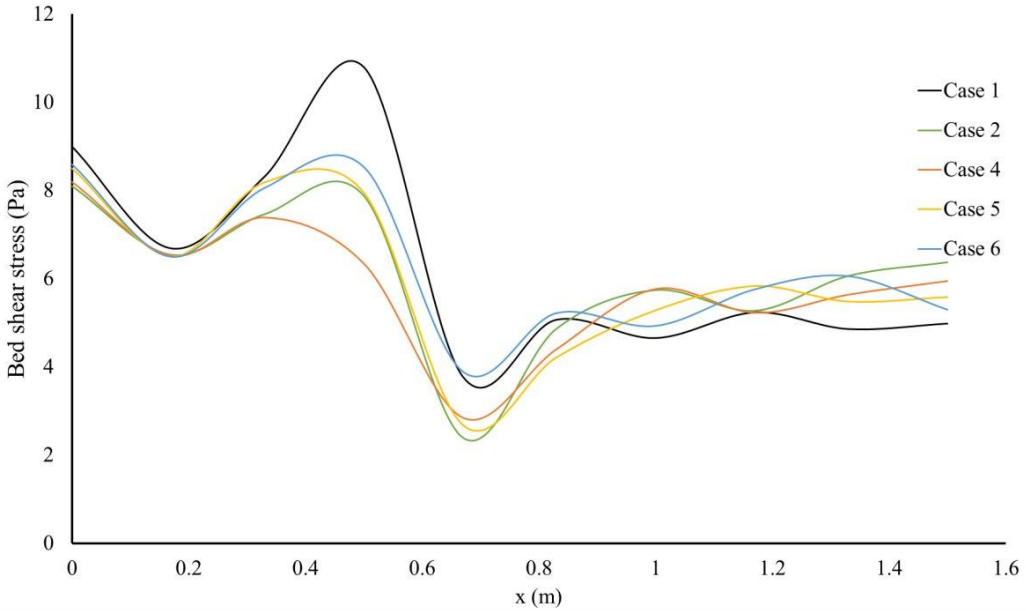

Figure 4.17: The average bed shear stress throughout the domain. The cylinder is located at $x = 0.35 - 0.45$ m

along the length of the channel for Case 1. The peak value of the bed shear stress occurred immediately downstream of the cylinder. The peak value was $11Pa$. For Cases 2, 4, 5 and 6, one can notice that the use of a splitter plate at either the downstream or the upstream side of cylinder could effectively reduce the bed shear stress around the cylinder, compared to Case 1. However, the curve for Case 4 shows the most effective decrease in the bed shear stress. The peak value of the bed shear stress dropped to 7.39 Pa. In other words, Case 4 reduced the peak bed shear stress by 32.8%. The interesting point of Case 4 is that the peak bed shear stress occur immediately in front of the cylinder. For Cases 2, 5 and 6, the peak bed shear stresses appeared immediately downstream of the cylinder. Cases 2, 5 and 6 gave approximately the same performance in terms of diminishing the peak bed shear stress. Downstream of the locations of the peak bed shear stress values for all cases (1, 2, 4, 5 and 6), the bed shear stresses decreased to the minimum values. Cases 2, 4 and 5 demonstrated effectiveness in achieving the minimum value. Further downstream, at increasing distance from the cylinder, the bed shear stresses for all the cases (1, 2, 4, 5 and 6) gradually increased to the value of around 5 Pa. Overall, Case 4 appeared to be the most effective case to decrease the bed shear stress around the cylinder.

4.5 Eddy Viscosity

The eddy viscosity is a property of the flow, not the fluid. It is the ratio of Reynolds shear stress within the turbulent flow of water to the velocity shear. The higher the eddy viscosity, the more significant the sediment transport.

For Case 1, Figure 4.18 shows that immediately downstream of the cylinder there was a region of high eddy viscosity. This region (red color) is likely to be subject to scour. Downstream of this region the eddy viscosity decreased. We are interested in suppressing eddy viscosity just downstream of the cylinder, therefore the eddy viscosity downstream of the cylinder fitted with a splitter plate at the downstream or the upstream side was investigated.

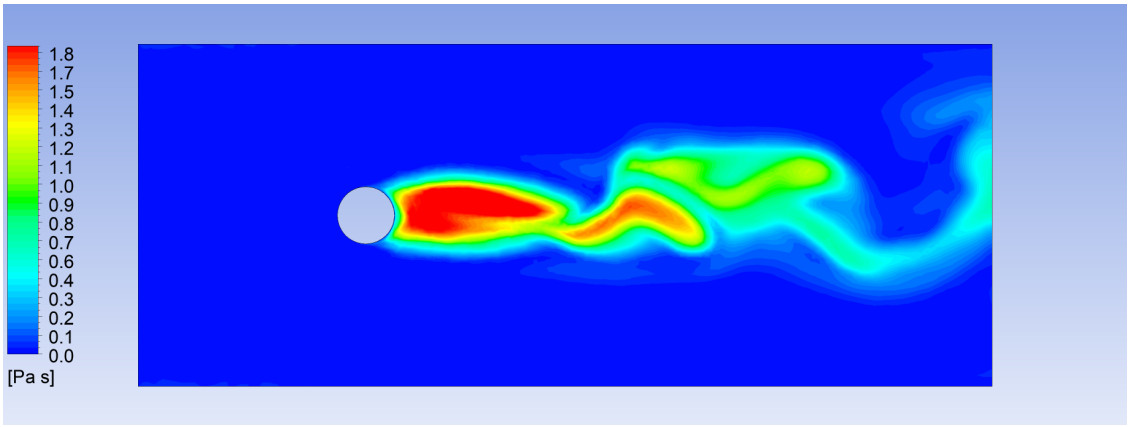

Figure 4.18: The horizontal plane at vertical distance of 2 cm above the bed, showing distributions of eddy viscosity for Case 1

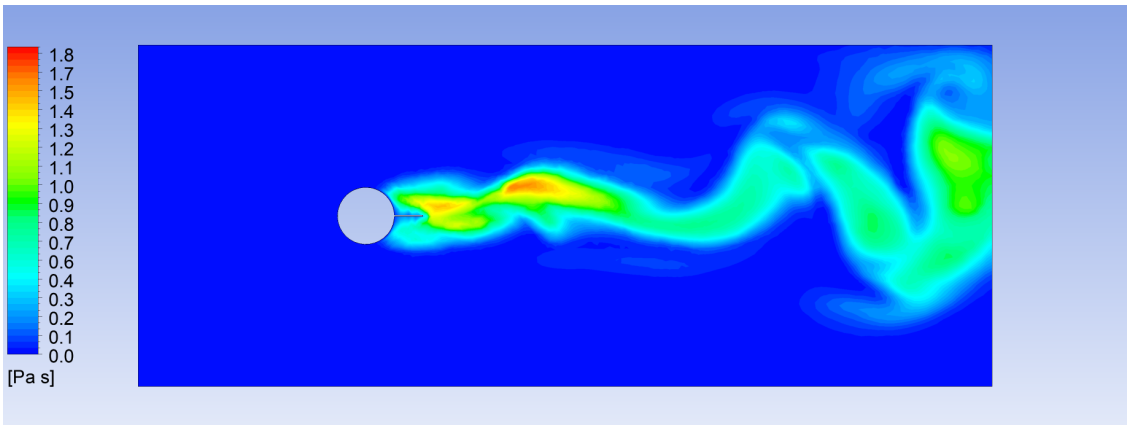

Figure 4.19: The horizontal plane at vertical distance of 2 cm above the bed, showing distributions of eddy viscosity for Case 2.

In Figures 4.19 and 4.20, Cases 2 and 4 are shown to be capable of reducing most of the high eddy viscosity region compared to Case 1. Case 4 is seen to shift the region of relatively high eddy viscosity towards downstream of the cylinder.

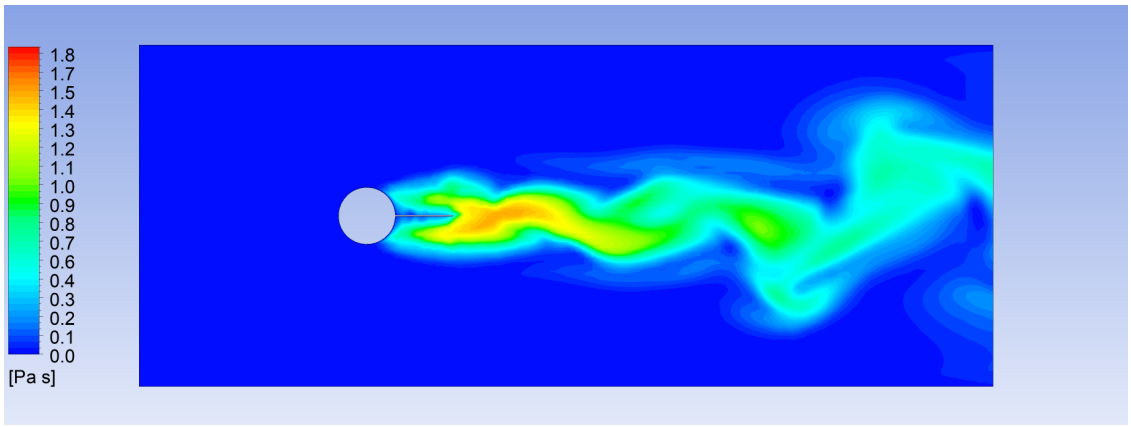

Figure 4.20: The horizontal plane at vertical distance of 2 cm above the bed, showing distributions of eddy viscosity for Case 4.

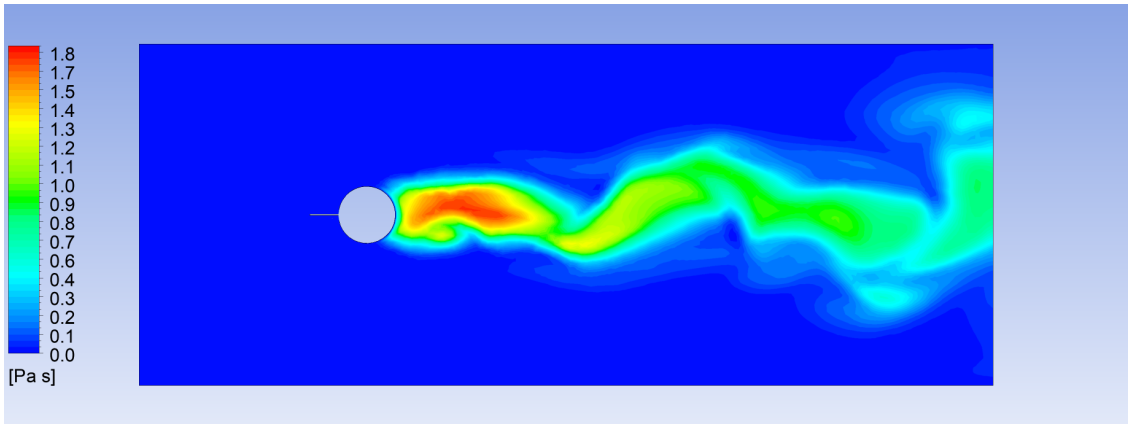

Figure 4.21: The horizontal plane at vertical distance of 2 cm above the bed, showing distributions of eddy viscosity for Case 5.

Both Cases 5 and 6 are reduced the high eddy viscosity regions in comparison to Case 1 but they are not as effective as Cases 2 and 4. Case 4 reduce greatly the region of high eddy viscosity.

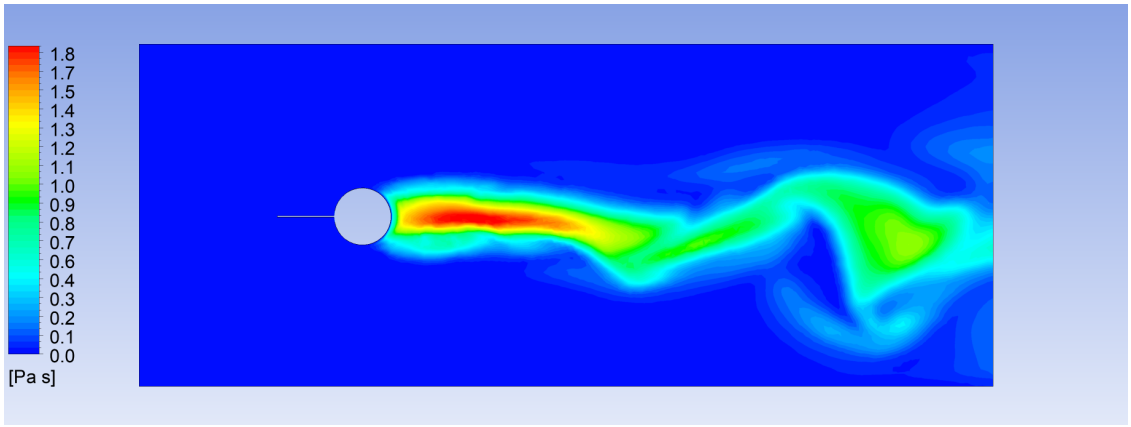

Figure 4.22: The horizontal plane at vertical distance of 2 cm above the bed, showing distributions of eddy viscosity for Case 6.

4.6 Turbulence eddy frequency

Turbulence eddy frequency (F) is the number of eddies occurring per second. Therefore, the unit of F is 1/s. Eddy frequency is essential when considering small-sized bridge piers or bridge piers made up of wood or weaker materials. High eddy frequency around these kinds of bridge piers would cause significant vibrations and ultimately causes damage to the bridge. Therefore, finding a way to decrease the high volume of eddy frequency is important. For Case 1, F had high values at the upstream side and close to the cylinder until the separation point. The separation points are identified on Figure 4.23. For cases 2, 4, 5 and 6, F was significantly reduced by fitting a splitter plate either at the downstream or upstream side of the cylinder. However, F had relatively high values in the region close to the separation point.

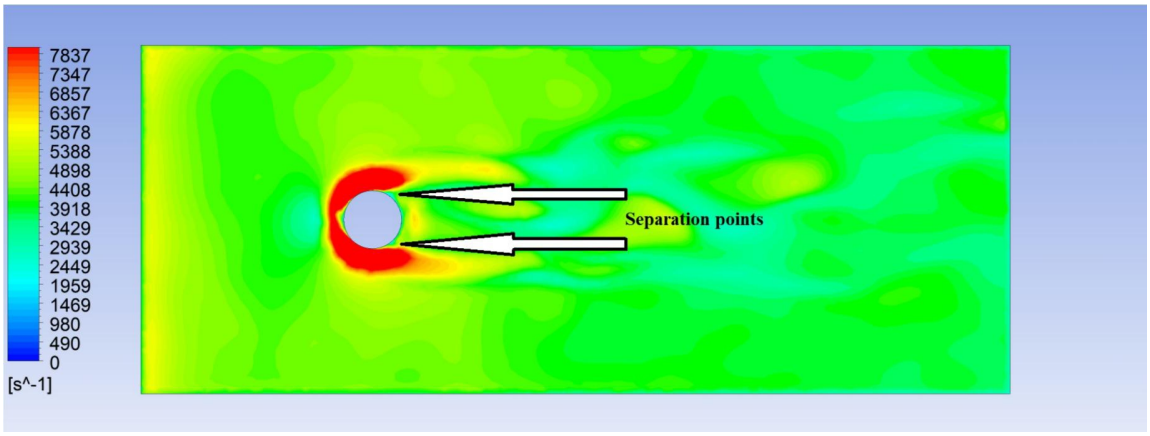

Figure 4.23: Contours of turbulence eddy frequency in the horizontal plane at a vertical distance of 2 cm from the bed level for Case 1.

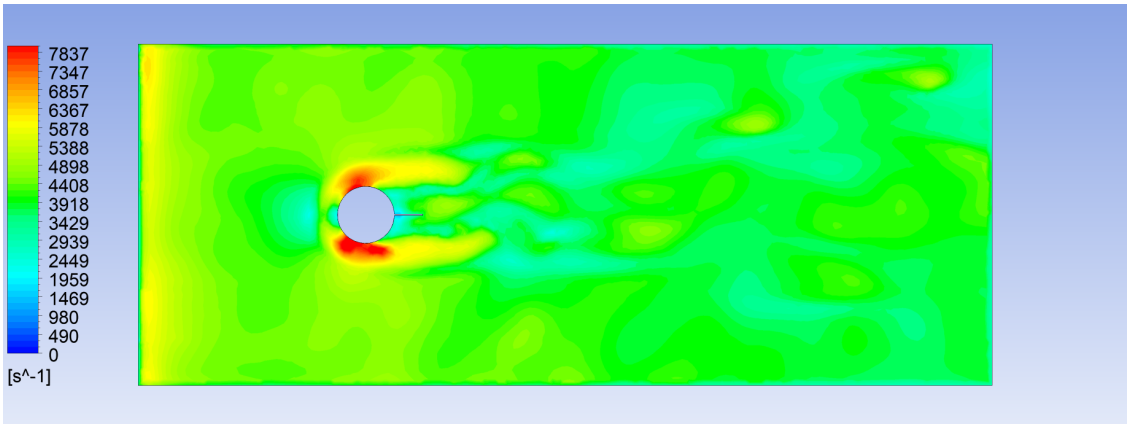

Figure 4.24: Contours of turbulence eddy frequency in the horizontal plane at a vertical distance of 2 cm from the bed level for Case 2.

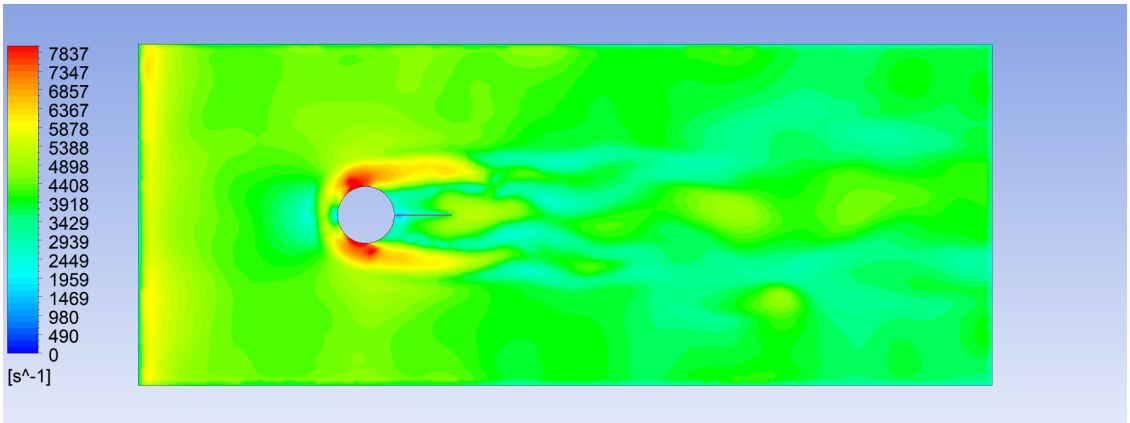

Figure 4.25: Contours of turbulence eddy frequency in the horizontal plane at a vertical distance of 2 cm from the bed level for Case 4.

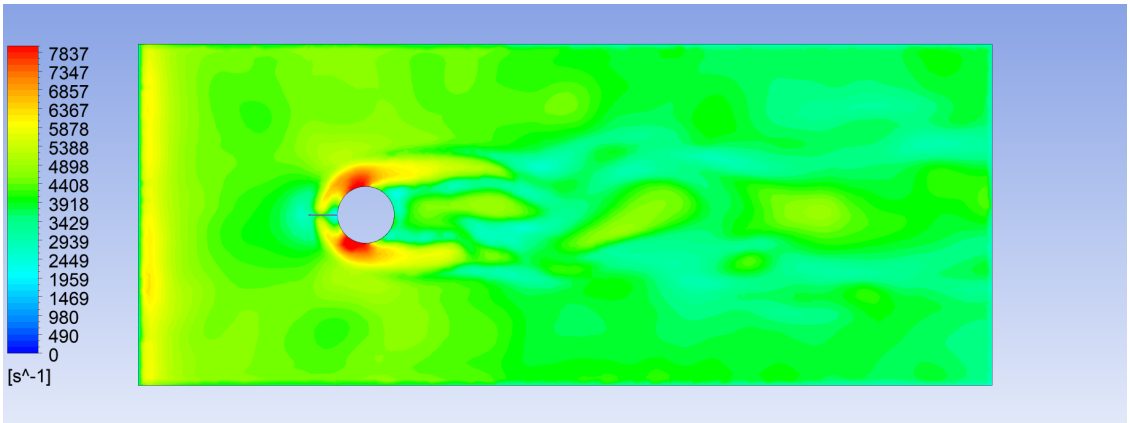

Figure 4.26: Contours of turbulence eddy frequency in the horizontal plane at a vertical distance of 2 cm from the bed level for Case 5.

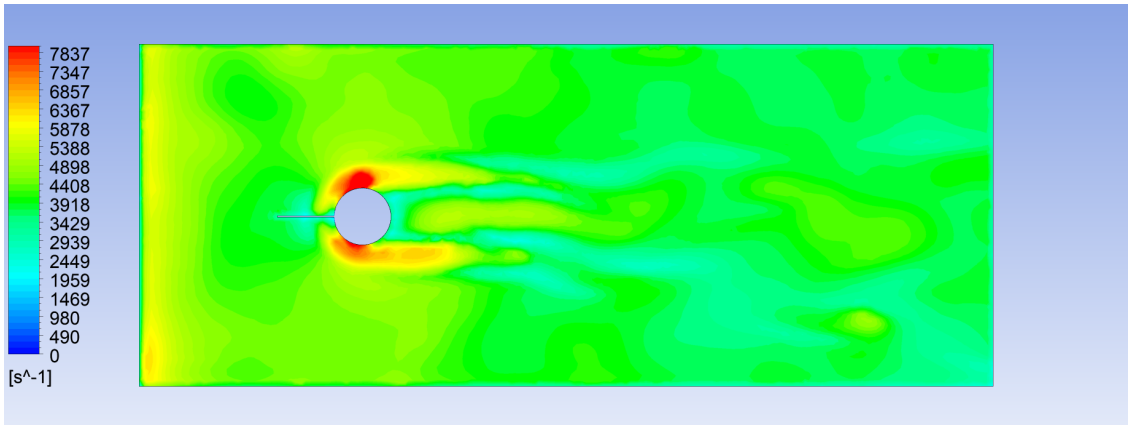

Figure 4.27: Contours of turbulence eddy frequency in the horizontal plane at a vertical distance of 2 cm from the bed level for Case 6.

4.7 Cross-channel velocity in the middle vertical plane

The Velocities in the z-direction (cross-channel direction) in the middle vertical plane (Figure 4.28) are discussed in this study. It is desirable to suppress the z-direction velocities as much as possible, because this will reduce the vibrations of the cylinder and help suppress the turbulent intensity. The red regions in Figures 4.29, 4.30, 4.31, 4.32 and 4.33 indicate z-direction velocities coming out of the paper and blue regions indicate z-direction velocities going into the paper.

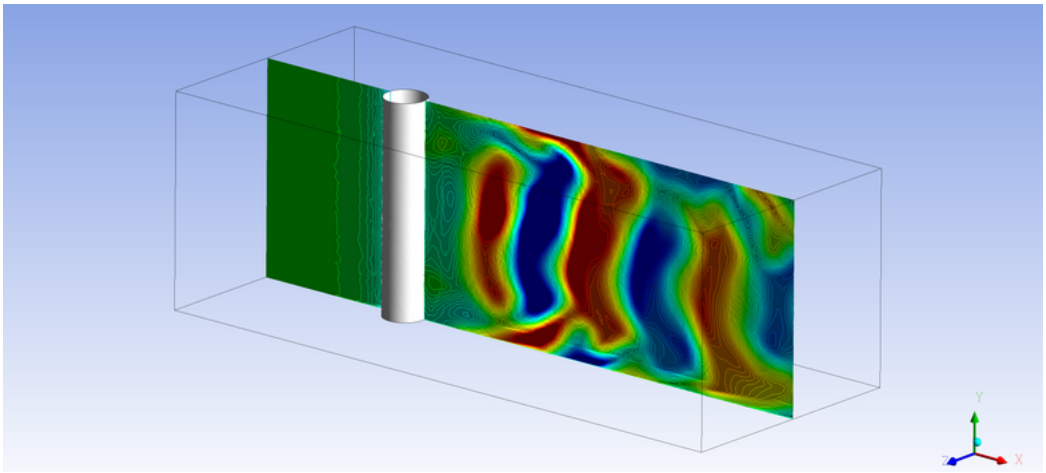

Figure 4.28: 3D view of the middle vertical plane

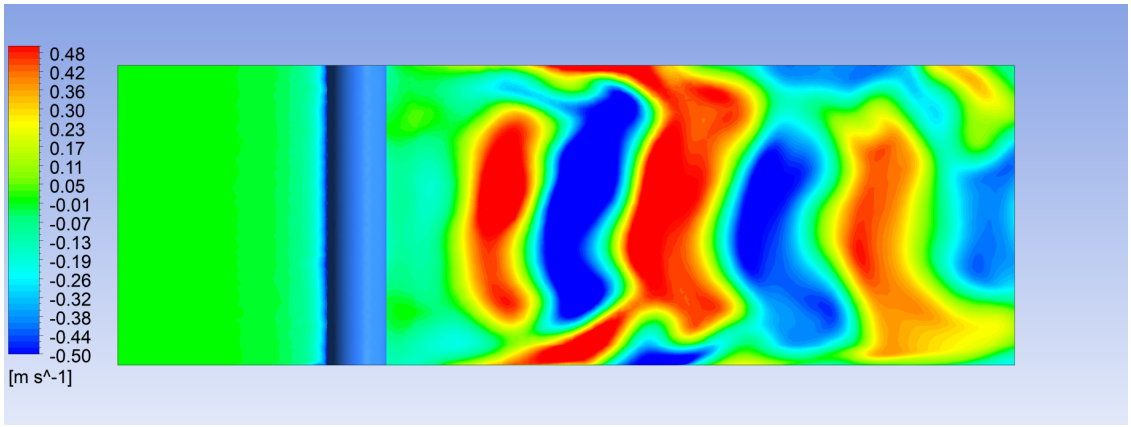

Figure 4.29: Distributions of cross-channel velocities for Case 1.

For Case 1 (Figure 4.29, the alternating red and blue regions extend from the surface to the bed level, showing the existence of vortices with high velocities downstream of the cylinder. The high velocities pointed at opposite directions with destructive impacts on the bed. The high velocities in the positive z-direction are visible from Figure 4.29, acting on the bed. This would enhance sediment transport and bed scouring.

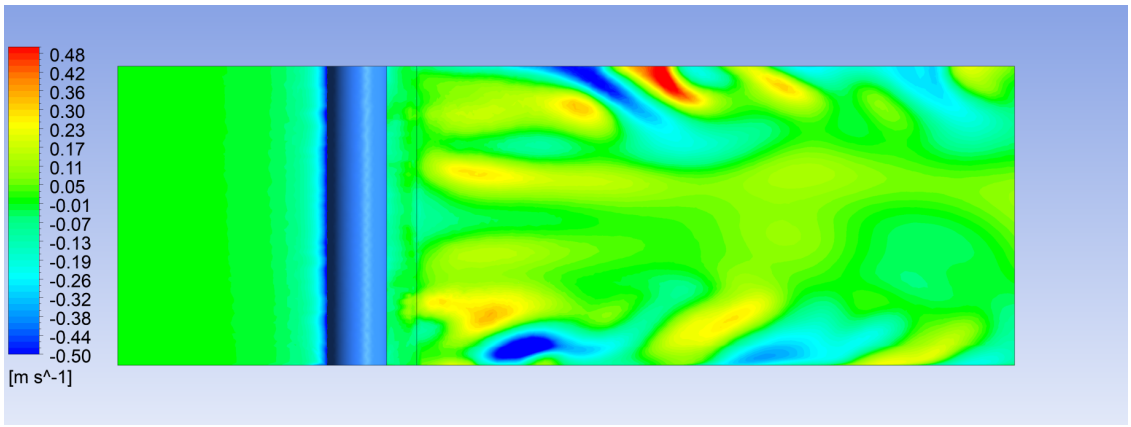

Figure 4.30: Distributions of cross-channel velocities for Case 2.

In Figure 4.30 for Case 2 (3.2), adding a plate of 0.5D in length reduced the regions of high back and forth velocities in the z-direction although ther was a small region (blue color near the bed) of high velocities going into the paper. Some high velocity regions

remained to be seen near the water surface but the motions were far away from the bed and also from the cylinder. Therefore, they are of low importance for the bed scour issues.

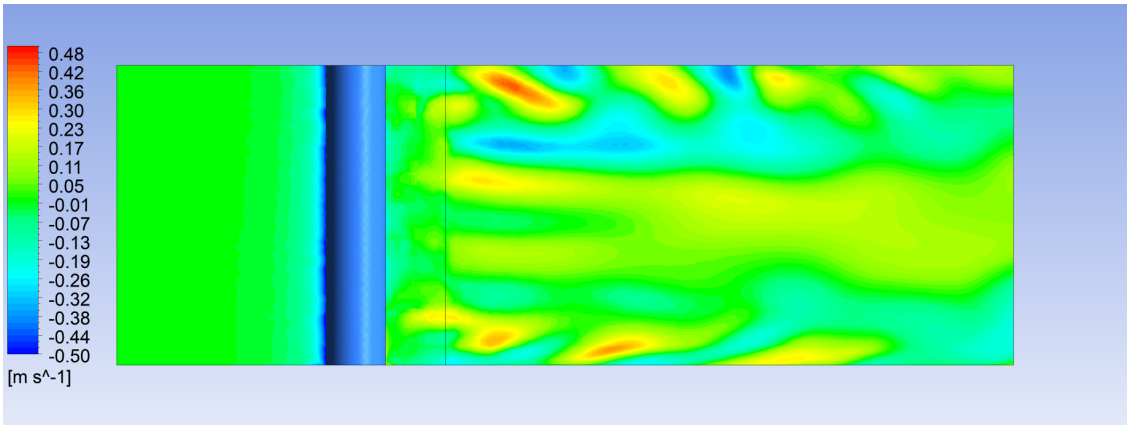

Figure 4.31: Distributions of cross-channel velocities for Case 4.

From Figure 4.31 for Case 4, one can notice suppressions of all vortices downstream of the cylinder. All of the red and blue regions in Figure 4.29 and 4.30 for Cases 1 and 2 did not appear in Figure 4.31 for Case 4.

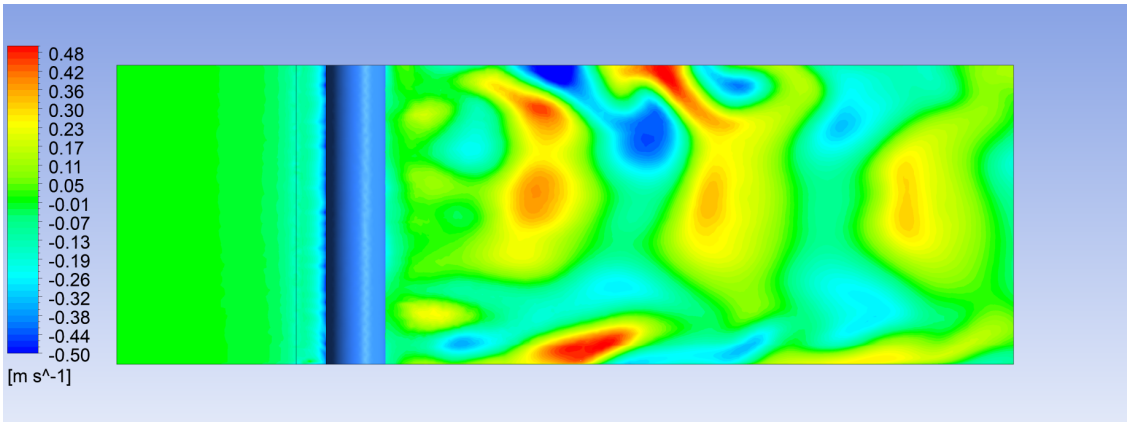

Figure 4.32: Distributions of cross-channel velocities for Case 5.

For Case 5, the velocities in the z-direction were reduced compared to Case 1. A comparison of Cases 2 and 4 to Case 5, it is clear that Case 5 is not as capable as Cases 2 and 4 in suppressing the velocities in z-direction. Some regions of red and blue still exist

near the bed level, which has important implications.

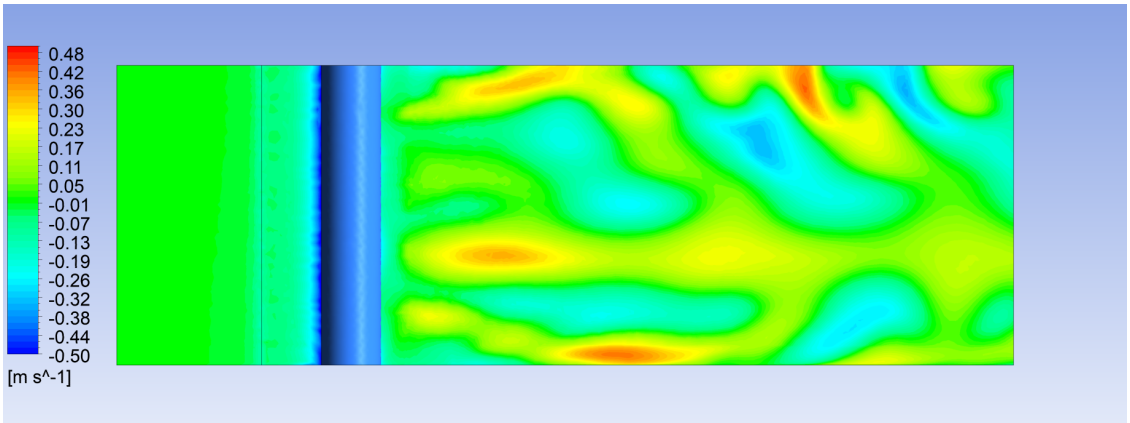

Figure 4.33: Distributions of cross-channel velocities for Case 6.

A comparison of Case 6 with Cases 2, 4 and 5 indicates that Case 6 is better than Cases 2 and 5, in terms of suppressing the velocities in z-direction. Cases 6 and 4 gave approximately the same performance. In conclusion, both Cases 4 and 6 are highly capable of reducing vortices and therefore, minimizing the velocities in the z-direction at the downstream side of the cylinder.

4.8 Vorticity

Figures 4.34, 4.35, 4.36, 4.37 and 4.38 show contours of vorticity in the horizontal plane at a vertical distance of 2cm from the bed level. All Cases (C1, C2, C4, C5 and C6) show a region of high vorticity at the wake of the cylinder and close to the cylinder. C1 shows more fluctuation at the downstream of the cylinder with multiple regions of high vorticity. C2 and C4 show less fluctuation in the downstream compared to C5 and C6.

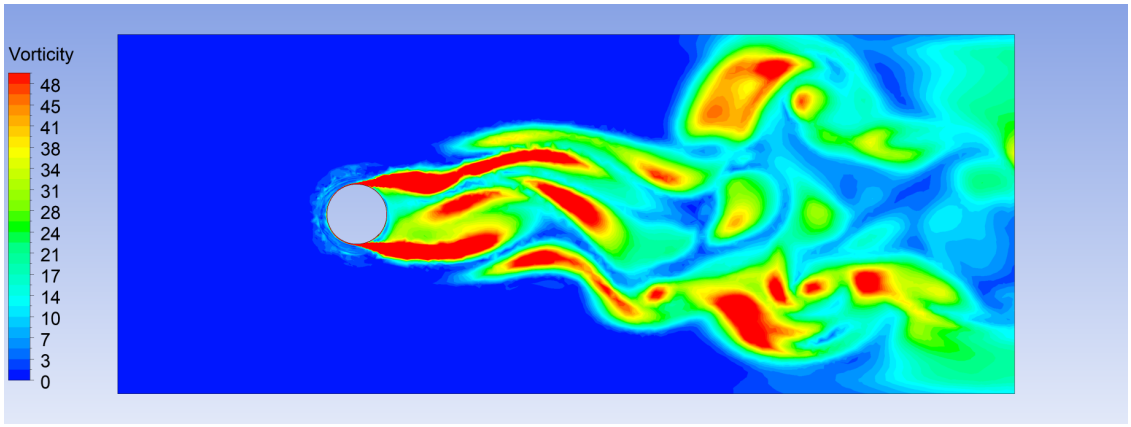

Figure 4.34: Contours of vorticity in the horizontal plane at a vertical distance of 2 cm from the bed level for Case 1.

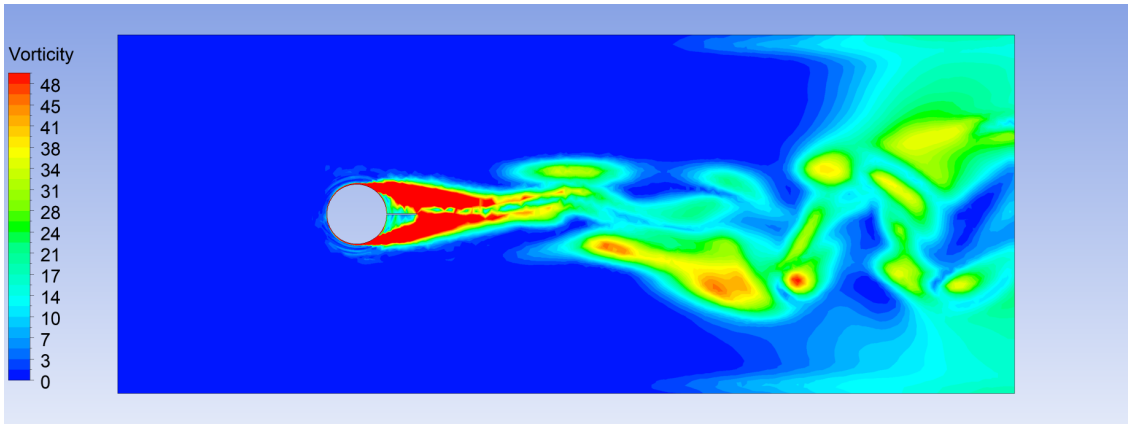

Figure 4.35: Contours of vorticity in the horizontal plane at a vertical distance of 2 cm from the bed level for Case 2.

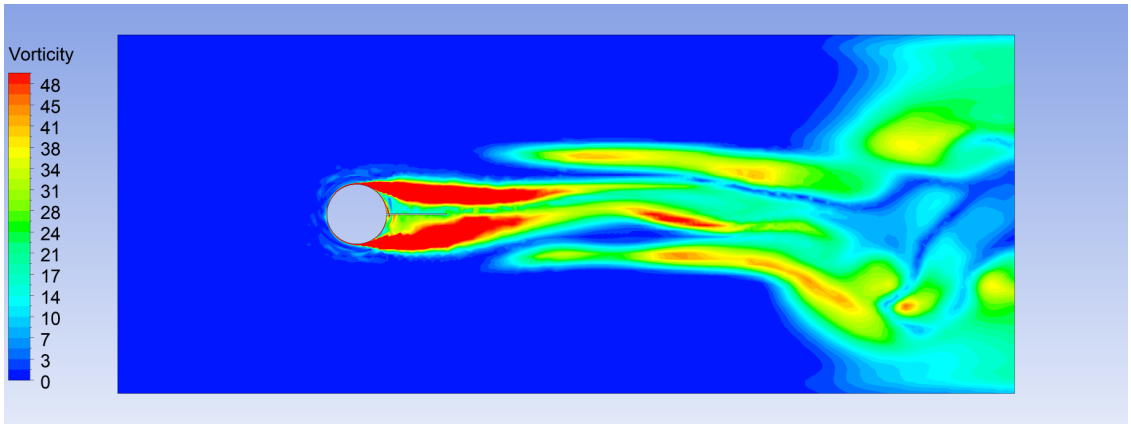

Figure 4.36: Contours of vorticity in the horizontal plane at a vertical distance of 2 cm from the bed level for Case 4.

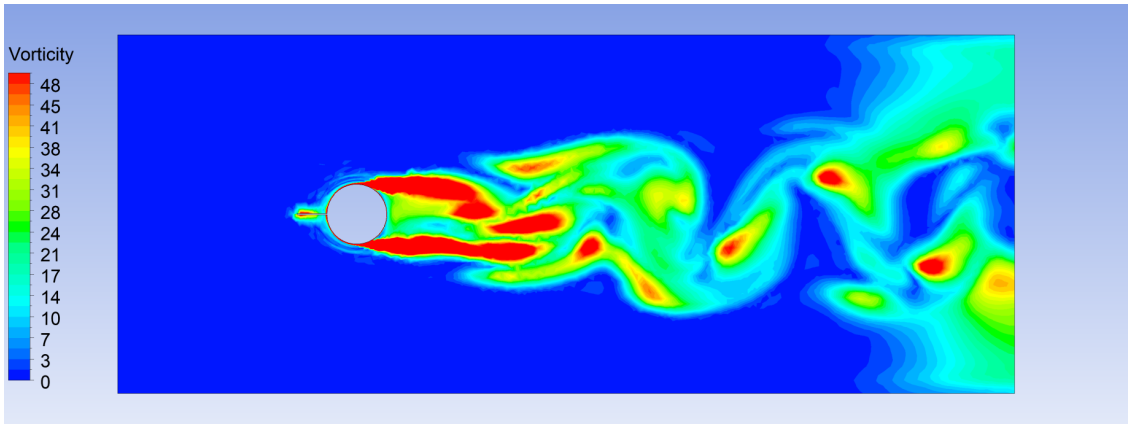

Figure 4.37: Contours of vorticity in the horizontal plane at a vertical distance of 2 cm from the bed level for Case 5.

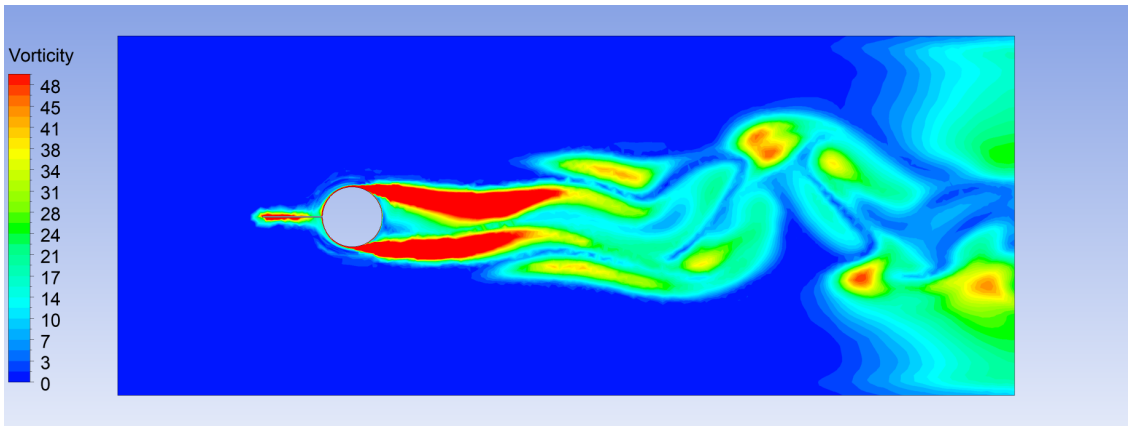

Figure 4.38: Contours of vorticity in the horizontal plane at a vertical distance of 2 cm from the bed level for Case 6.

Chapter 5

Conclusions and suggestions for further research

5.1 Concluding remarks

This thesis presents numerical simulations of turbulent flow around a cylinder. The numerical results of drag and lift coefficients are obtained and compared with the results from an independent source. The numerical simulations cover both the case of a bare cylinder and cases of a cylinder fitted with a splitter plate on the upstream or downstream side. An analysis of the numerical results has reached the following conclusions:

(1) For a reduction of drag coefficient $\overline{C}_D$ values, fitting a splitter plate on the upstream side of the cylinder (Runs C5 and C6, listed in Table 3.2) is the most effective, compared to the cases of no splitter plate (Run C1) and of a splitter plate fitted on the downstream side (Runs C2–C4). The $\overline{C}_D$ values for C5 and C6 drop to 0.48 and 0.49, respectively, which are a reduction of approximately 45% from the case of C1. The values of $\overline{C}_D$ for C1 and C3 are in agreement with the results of Dai et al. (2018). A reduction of the drag coefficient means reduced drag forces exerted by the flow on

piers.

(2) Regarding the lift coefficient, the C_l' values decrease by 79 – 82% by fitting a splitter plate on the downstream side of the cylinder (Runs C2 and C4), compared to the case of no splitter plate (Run C1). Lift forces would cause vibrations on piers and increase vortex shedding power. This finding has implications for the design of in-stream bridge piers and deserves the attention of design engineers. The case of Run C4 appears desirable with respect to reducing both drag and lift forces. This finding is a new contribution.

(3) In the absence of a splitter plate (Run C1), the peak value of turbulence kinetic energy occurs immediately downstream of the cylinder. The numerical results for C1 gives a peak value of $K = 0.142$ m^2/s^2. Fitting a splitter plate on the downstream side of the cylinder (Run C4) reduces the peak value to 0.087 m^2/s^2. This is a 39% reduction. The reduced peak value shifts location towards downstream. This finding is in agreement with those of De Araujo et al. (2018) and Ozkan et al. (2017). A reduction of K values helps reduce the erosion of channel-bed sediments by turbulent flow.

(4) The channel-bed shear stresses vary around the cylinder, and their spatial distributions show maximum and minimum values on the downstream side. Without a splitter plate (Run C1), the maximum value reaches 11 Pa. Fitting a splitter plate on the downstream of the cylinder (Run C4) reduces the maximum value by 33% to 7.4 Pa; it also reduces the minimum value by 28%. A reduction of channel-bed shear stresses has beneficial effects, preventing channel-bed sediments from suspension and erosion, and controlling water turbidity.

(5) Turbulent eddy viscosity is an indicator of the strength of eddy motions. Fitting a splitter plate on the downstream side of the cylinder (Runs C2 and C4) is more

effective in reducing the magnitude of turbulent eddy viscosity than fitting a splitter plate on the upstream side (Runs C5 and C6).

(6) The absence of a splitter plate (Run C1) incurs high values of turbulence eddy frequency (Figure 4.23). A splitter plate fitted on either the upstream or downstream side of the cylinder (Runs C2, and C4 – C6) has the capability to reduce turbulence eddy frequency in the vicinity of the cylinder. However, there still exist regions of relatively high turbulence eddy frequency in the points of flow separation, even in the presence of a splitter plate.

(7) In the absence of a splitter plate (Run C1), alternating high flow velocities in the cross-channel direction take place in the channel-centre plane (Figure 4.29). This is undesirable. The presence of a splitter plate (Runs C2, and C4 – C6) produces an improvement. C4 and C6 (Table 4.1) give the best improvement of suppressing the high flow velocities.

5.2 Future work

Future studies should investigate

- the effect of a larger splitter plate fitted on both the upstream and downstream sides of a cylinder;
- flow turbulence in the presence of a scour hole around a cylinder;
- situations where bridge piers have different shapes;
- experimentally flow turbulence at high Reynolds numbers over a mobile channel-bed around one or more piers.

All these are a challenging task.

References

Abdi, R., Rezazadeh, N., & Abdi, M. (2017, 03). Reduction of fluid forces and vortex shedding frequency of a circular cylinder using rigid splitter plates. *European Journal of Computational Mechanics*, *26*, 1-20. doi: 10.1080/17797179.2017.1306826

Akilli, H., Karakus, C., Akar, A., Sahin, B., & Tumen, N. F. (2008, 04). Control of Vortex Shedding of Circular Cylinder in Shallow Water Flow Using an Attached Splitter Plate. *Journal of Fluids Engineering*, *130*(4). Retrieved from https://doi.org/10.1115/1.2903813 (041401) doi: 10.1115/1.2903813

Ali, K. H. M., & Karim, O. (2002). Simulation of flow around piers. *Journal of Hydraulic Research*, *40*(2), 161-174. Retrieved from https://doi.org/10.1080/00221680209499859 doi: 10.1080/00221680209499859

An, X., Song, B., Tian, W.-l., & Ma, C. (2019, 02). Numerical research of flow past a circular cylinder with splitter plate at a subcritical reynolds number region. *Journal of Shanghai Jiaotong University (Science)*, *24*, 113-121. doi: 10.1007/s12204-019-2045-y

Ansys 2019b. (n.d.). Retrieved from https://www.ansys.com/products/fluids/ansys-fluent

Apelt, C. J., & West, G. S. (1975). The effects of wake splitter plates on bluff-body flow in the range 104 lt; r lt; 5 104. part 2. , 145–160.

Arneson, L. (2013). *Evaluating scour at bridges* (Tech. Rep.). United States. Federal Highway Administration.

Bearman, P., & Branković, M. (2004). Experimental studies of passive control of vortex-induced vibration. *European Journal of Mechanics - B/Fluids*, *23*(1), 9 - 15. Retrieved from http://www.sciencedirect.com/science/article/pii/S0997754603000840 (Bluff Body Wakes and Vortex-Induced Vibrations) doi: https://doi.org/10.1016/j.euromechflu.2003.06.002

Boussinesq, J. (1887). *Cours d'analyse infinitésimale en vue des applications mécaniques et physiques*. Gauthier-Villars: Paris, France.

Bradshaw, P. (2003). Turbulent flow: Analysis, measurement and prediction. by p. s. bernard amp; j. m. wallace. wiley, 2002. 1999. 497 pp. isbn 0 471 33219 4. *Journal of Fluid Mechanics*, *478*, 344–345. doi: 10.1017/S0022112002003464

Chen, W., Xin, F., D.B.and Xu, & Li, J. H. H., H.and Ou. (2013). Suppression of vortex-induced vibration of a circular cylinder using suction-based flow control. (42).

Choi, S.-U., & Choi, B. (2016, 02). Prediction of time-dependent local scour around bridge piers. *Water and Environment Journal*, *30*, n/a-n/a. doi: 10.1111/wej.12157

Chutkey, K., Suriyanarayanan, P., & Venkatakrishnan, L. (2018). Near wake field of circular cylinder with a forward splitter plate. *Journal of Wind Engineering and Industrial Aerodynamics*, *173*, 28 - 38. Retrieved from http://www.sciencedirect.com/science/article/pii/S0167610517302398 doi: https://doi.org/10.1016/j.jweia.2017.11.019

Concordia hpc. (n.d.). Retrieved from https://www.concordia.ca/ginacody/aits/speed.html

Da Silva, B. L., Luciano, R. D., Utzig, J., & Meier, H. F. (2019). Analysis of flow behavior and fluid forces in large cylinder bundles by numerical simulations. *International Journal of Heat and Fluid Flow*, *75*, 209 - 226. Retrieved from http://www.sciencedirect.com/science/article/pii/S0142727X18306416 doi: https://doi.org/10.1016/j.ijheatfluidflow.2019

.01.006

Dai, S., Younis, B. A., Zhang, H., & Guo, C. (2018). Prediction of vortex shedding suppression from circular cylinders at high reynolds number using base splitter plates. *Journal of Wind Engineering and Industrial Aerodynamics*, *182*, 115 - 127. Retrieved from http://www.sciencedirect.com/science/article/pii/S0167610518303295 doi: https://doi.org/10.1016/j.jweia.2018.09.006

Dargahi, B. (1989). The turbulent flow field around a circular cylinder. *Experiments in Fluids*, *8*, 1-12.

Dash, S. M., Triantafyllou, M. S., & Alvarado, P. V. Y. (2020). A numerical study on the enhanced drag reduction and wake regime control of a square cylinder using dual splitter plates. *Computers Fluids*, *199*, 104421. Retrieved from http://www.sciencedirect.com/science/article/pii/S0045793019303792 doi: https://doi.org/10.1016/j.compfluid.2019.104421

De Chant, L. J. (2005). The venerable 1/7th power law turbulent velocity profile: a classical nonlinear boundary value problem solution and its relationship to stochastic processes. *Applied Mathematics and Computation*, *161*(2), 463 - 474. Retrieved from http://www.sciencedirect.com/science/article/pii/S0096300304000050 doi: https://doi.org/10.1016/j.amc.2003.12.109

De Araujo, L., Camano Schettini, E., & Silvestrini, J. (2016, 09). Direct numerical simulation of turbulent flow past a cylinder with splitter plate..

De Araujo, L., Camano Schettini, E., & Silvestrini, J. (2018, 06). Direct numerical simulation of the flow around a cylinder with splitter plate: analysis for moderated reynolds numbers. *Journal of the Brazilian Society of Mechanical Sciences and Engineering*, *40*. doi: 10.1007/s40430-018-1199-0

Dias, A. J., Fael, C. S., & Nunez-Gonzalez, F. (2019, feb). Effect of debris on the local

scour at bridge piers. *IOP Conference Series: Materials Science and Engineering*, *471*, 022024. Retrieved from https://doi.org/10.1088%2F1757-899x%2F471%2F2%2F022024 doi: 10.1088/1757-899x/471/2/022024

Ettema, R., Kirkil, G., & Muste, M. (2006, 01). Similitude of large-scale turbulence in experiments on local scour at cylinders. *Journal of Hydraulic Engineering-asce - J HYDRAUL ENG-ASCE*, *132*. doi: 10.1061/(ASCE)0733-9429(2006)132:1(33)

Ettema, R., Melville, B. W., & Barkdoll, B. (1998). Scale effect in pier-scour experiments. *Journal of Hydraulic Engineering*, *124*(6), 639–642.

Graf, W., & Istiarto, I. (2002). Flow pattern in the scour hole around a cylinder. *Journal of Hydraulic Research*, *40*(1), 13-20. Retrieved from https://doi.org/10.1080/00221680209499869 doi: 10.1080/00221680209499869

Guan, D., Chiew, Y.-M., Wei, M., & Hsieh, S.-C. (2019). Characterization of horseshoe vortex in a developing scour hole at a cylindrical bridge pier. *International Journal of Sediment Research*, *34*(2), 118 - 124. Retrieved from http://www.sciencedirect.com/science/article/pii/S1001627917303815 doi: https://doi.org/10.1016/j.ijsrc.2018.07.001

Homescu, C., Navon, I. M., & Li, Z. (2002). Suppression of vortex shedding for flow around a circular cylinder using optimal control. *International Journal for Numerical Methods in Fluids*, *38*(1), 43-69. Retrieved from https://onlinelibrary.wiley.com/doi/abs/10.1002/fld.203 doi: 10.1002/fld.203

https://guardian retentionsystems.com/bridge-piers/. (n.d.). Retrieved from https://guardianretentionsystems.com/bridge-piers/

Huang, W., Yang, Q., & Xiao, H. (2009, 05). Cfd modeling of scale effects on turbulence flow and scour around bridge piers. *Computers Fluids*, *38*, 1050-1058. doi: 10.1016/j.compfluid.2008.01.029

Jia, Y., Altinakar, M., & Guney, M. S. (2018). Three-dimensional numerical simulations of

local scouring around bridge piers. *Journal of Hydraulic Research*, *56*(3), 351-366. Retrieved from https://doi.org/10.1080/00221686.2017.1356389 doi: 10.1080/00221686.2017.1356389

Jones, W., & Launder, B. (1972). The prediction of laminarization with a two-equation model of turbulence. *International Journal of Heat and Mass Transfer*, *15*(2), 301 - 314. Retrieved from http://www.sciencedirect.com/science/article/pii/0017931072900762 doi: https://doi.org/10.1016/0017-9310(72)90076-2

Khaple, S., Hanmaiahgari, P., Gaudio, R., & Dey, S. (2017, 09). Splitter plate as a flow-altering pier scour countermeasure. *Acta Geophysica*, *65*. doi: 10.1007/s11600-017-0084-z

Kwon, S., Cho, J., Park, J., & Choi, H. (2002). The effects of drag reduction by ribbons attached to cylindrical pipes. *Ocean Engineering*, *29*(15), 1945 - 1958. Retrieved from http://www.sciencedirect.com/science/article/pii/S0029801802000100 doi: https://doi.org/10.1016/S0029-8018(02)00010-0

Lecordier, J. C., Hamma, L., & Paranthoen, P. (1991, Jan 01). The control of vortex shedding behind heated circular cylinders at low reynolds numbers. *Experiments in Fluids*, *10*(4), 224–229. Retrieved from https://doi.org/10.1007/BF00190392 doi: 10.1007/BF00190392

Liu, K., Deng, J., & Mei, M. (2016). Experimental study on the confined flow over a circular cylinder with a splitter plate. *Flow Measurement and Instrumentation*, *51*, 95 - 104. Retrieved from http://www.sciencedirect.com/science/article/pii/S095559861630139X doi: https://doi.org/10.1016/j.flowmeasinst.2016.09.002

Melville, B. (1997). Pier and abutment scour: Integrated approach..

Menter, F. R. (1994). Two-equation eddy-viscosity turbulence models for engineering applications. *AIAA Journal*, *32*(8), 1598-1605. Retrieved from https://doi.org/10.2514/3.12149 doi: 10.2514/3.12149

Nguyen, T. H. T., Ahn, J., & Park, S. W. (2018). Numerical and physical investigation of the performance of turbulence modeling schemes around a scour hole downstream of a fixed bed protection. *Water*, *10*, 103.

Ozkan, G. M., Firat, E., & Akilli, H. (2017). Passive flow control in the near wake of a circular cylinder using attached permeable and inclined short plates. *Ocean Engineering*, *134*, 35 - 49. Retrieved from http://www.sciencedirect.com/science/article/pii/S0029801817300756 doi: https://doi.org/10.1016/j.oceaneng.2017.02.014

Pasiok, R., & Stilger-szydlo, E. (2010). Sediment particles and turbulent flow simulation around bridge piers. *Archives of Civil and Mechanical Engineering*, *10*(2), 67 - 79. Retrieved from http://www.sciencedirect.com/science/article/pii/S164496651260051X doi: https://doi.org/10.1016/S1644-9665(12)60051-X

Qiu, Y., Sun, Y., Wu, Y., & Tamura, Y. (2014). Effects of splitter plates and reynolds number on the aerodynamic loads acting on a circular cylinder. *Journal of Wind Engineering and Industrial Aerodynamics*, *127*, 40-50.

Richardson, E., & Davis, S. (2001). Evaluating scour at bridges. , *124*(18).

Sadeque, M. A., Rajaratnam, N., & Loewen, M. R. (2008). Flow around cylinders in open channels. *Journal of Engineering Mechanics*, *134*(1), 60-71. doi: 10.1061/(ASCE)0733-9399(2008)134:1(60)

Salaheldin, T. M., Imran, J., & Chaudhry, M. H. (2004). Numerical modeling of three-dimensional flow field around circular piers. *Journal of Hydraulic Engineering*, *130*(2), 91-100. doi: 10.1061/(ASCE)0733-9429(2004)130:2(91)

Schumm, M., Berger, E., & Monkewitz, P. A. (1994). Self-excited oscillations in the wake of two-dimensional bluff bodies and their control. *Journal of Fluid Mechanics*, *271*, 17–53. doi: 10.1017/S0022112094001679

Shaligram, T., Chakraborty, Gautam, B., & Pradipta, P. (2005, 01). Numerical prediction of flow and heat transfer in a channel in the presence of a built-in circular tube with and without an integral wake splitter. *International Journal of Heat and Mass Transfer*, *48*, 439-453. doi: 10.1016/j.ijheatmasstransfer.2004.09.003

Smagorinsky, J. (1963, 03). General circulation experiments with the primitive equations: I. The basic experiment*. *Monthly Weather Review*, *91*(3), 99-164. Retrieved from https://doi.org/10.1175/1520-0493(1963)091<0099:GCEWTP>2.3.CO;2 doi: 10.1175/1520-0493(1963)091⟨0099:GCEWTP⟩2.3.CO;2

Soumya, S., & Prakash, K. A. (2017). Effect of splitter plate on passive control and drag reduction for fluid flow past an elliptic cylinder. *Ocean Engineering*, *141*, 351 - 374. Retrieved from http://www.sciencedirect.com/science/article/pii/S0029801817303347 doi: https://doi.org/10.1016/j.oceaneng.2017.06.034

Stahlmann, A. (2014, 05). Numerical and experimental modeling of scour at foundation structures for offshore wind turbines. , *1*, 131-138.

Vu, H., Ahn, J., & Hwang, J. (2015, 10). Numerical investigation of flow around circular cylinder with splitter plate. *KSCE Journal of Civil Engineering*, *20*. doi: 10.1007/s12205-015-0209-3

Wilcox, D. (1993). *Turbulence modelling for cfd*. DCW Industries, Inc.: La Canada, CA, USA.

Wilcox, D., et al. (1998). *Turbulence modeling for cfd* (Vol. 2). DCW industries La Canada, CA.

Wu, P., Balachandar, R., & Ramamurthy, A. (2018). Effects of splitter plate on reducing local scour around bridge pier. *River Research and Applications*, *34*(10), 1338-1346. Retrieved from https://onlinelibrary.wiley.com/doi/abs/10.1002/rra.3363 doi: 10.1002/rra.3363

www.researchgate.net. (n.d.). Retrieved from https://www.researchgate.net/publication/314359391_LiDAR_and_Field_Investigation_of_the_March_11_2011_M_90_Great_Tohoku_Offshore_Earthquake_and_April_7_2011_M_74_Aftershock/figures?lo=1

Yeh, J. (1996, 01). The flow fields around square and circular cylinders mounted vertically on a fixed flat bottom (in chinese) m.s. thesis. natiional chunng-hsing universit. , taichung.

Yen, C.-L., Lai, J.-S., & Chang, W.-Y. (2001, 01). Modeling of 3d flow and scouring around circular piers. , *25*, 17-26.

Zaid, M., Yazdanfar, Z., Chowdhury, H., & Alam, F. (2019). Numerical modeling of flow around a pier mounted in a flat and fixed bed. *Energy Procedia*, *160*, 51 - 59. Retrieved from http://www.sciencedirect.com/science/article/pii/S1876610219312020 (2nd International Conference on Energy and Power, ICEP2018, 13–15 December 2018, Sydney, Australia) doi: https://doi.org/10.1016/j.egypro.2019.02.118

Zhou, T., Razali, S. M., Hao, Z., & Cheng, L. (2011). On the study of vortex-induced vibration of a cylinder with helical strakes. *Journal of Fluids and Structures*, *27*(7), 903 - 917. Retrieved from http://www.sciencedirect.com/science/article/pii/S0889974611000776 doi: https://doi.org/10.1016/j.jfluidstructs.2011.04.014